JOINT TRANSPORTATION
RESEARCH PROGRAM
INDIANA DEPARTMENT OF TRANSPORTATION
AND PURDUE UNIVERSITY

Early Detection of Joint Distress in Portland Cement Concrete Pavements

Dwayne Harris

Yaghoob Farnam

Robert Spragg

Paul Imbrock

W. Jason Weiss

SPR-3623 • Report Number: FHWA/IN/JTRP-2015/09 • DOI: 10.5703/1288284315531

RECOMMENDED CITATION

Harris, D., Farnam, Y., Spragg, R., Imbrock, P., & Weiss, W. J. (2015). *Early detection of joint distress in portland cement concrete pavements* (Joint Transportation Research Program Publication No. FHWA/IN/JTRP-2015/09). West Lafayette, IN: Purdue University. http://dx.doi.org/10.5703/1288284315531

AUTHORS

Dwayne Harris, PhD, PE, LPG
Transportation Research Engineer
Division of Research and Development
Indiana Department of Transportation

Yaghoob Farnam, PhD
Postdoctoral Research Associate
Lyles School of Civil Engineering
Purdue University

Robert Spragg
Graduate Research Assistant
Lyles School of Civil Engineering
Purdue University

Paul Imbrock
Graduate Research Assistant
Lyles School of Civil Engineering
Purdue University

W. Jason Weiss, PhD
Jack and Kay Hockema Professor and Director of Pankow Materials Laboratory
Lyles School of Civil Engineering
Purdue University
(541) 737-1885
jasonweiss99@gmail.com
Corresponding Author

JOINT TRANSPORTATION RESEARCH PROGRAM

The Joint Transportation Research Program serves as a vehicle for INDOT collaboration with higher education institutions and industry in Indiana to facilitate innovation that results in continuous improvement in the planning, design, construction, operation, management and economic efficiency of the Indiana transportation infrastructure. https://engineering.purdue.edu/JTRP/index_html

Published reports of the Joint Transportation Research Program are available at: http://docs.lib.purdue.edu/jtrp/

NOTICE

COPYRIGHT

Print ISBN: 978-1-62260-350-3
ePUB ISBN: 978-1-62260-351-0

TECHNICAL REPORT STANDARD TITLE PAGE

1. Report No. FHWA/IN/JTRP-2015/09	**2. Government Accession No.**	**3. Recipient's Catalog No.**
4. Title and Subtitle Early Detection of Joint Distress in Portland Cement Concrete Pavements		**5. Report Date** March 2015
		6. Performing Organization Code
7. Author(s) Dwayne Harris, Yaghoob Farnam, Robert Spragg, Paul Imbrock, W. Jason Weiss		**8. Performing Organization Report No.** FHWA/IN/JTRP-2015/09
9. Performing Organization Name and Address Joint Transportation Research Program Purdue University 550 Stadium Mall Drive West Lafayette, IN 47907-2051		**10. Work Unit No.**
		11. Contract or Grant No. SPR-3623
12. Sponsoring Agency Name and Address Indiana Department of Transportation State Office Building 100 North Senate Avenue Indianapolis, IN 46204		**13. Type of Report and Period Covered** Final Report
		14. Sponsoring Agency Code

15. Supplementary Notes

Prepared in cooperation with the Indiana Department of Transportation and the Federal Highway Administration.

16. Abstract

INDOT (as well as several surrounding states) have observed that certain concrete pavements may show a susceptibility to joint deterioration. Unfortunately, by the time that this joint deterioration is observed it is often too late and costly partial depth repairs are needed. The deterioration is generally occurring in the joint behind the backer rod and joint sealant; as such, it is difficult to detect even if one is standing directly above the joint. This project investigated the use of electrical resistivity and ground penetrating radar as two techniques to detect premature joint deterioration. The thought process was that if the joint deterioration is determined at an early stage, low cost corrective actions can be taken to extend the life of the concrete. The electrical response was measured for mortars subjected to a temperature cycle from 23 °C to -35 °C, with varying degrees of saturation, and varying salt concentrations. The resistivity increased as the degree of saturation was reduced due to the reduction in the volume of the conductive medium and increase in tortuosity. Changes in resistivity were detected when cracking occurred in the sample. The magnitude of these changes was similar to that detected using changes in the ultrasonic wave speed. Ground penetrating radar (GPR) was used effectively to detect fluid accumulation in the saw-cut joint behind the joint sealant. The typical GPR waveforms are however difficult and time consuming to interpret. A signal processing approach called, referred to as the CID, was used to obtain a single number that reflects the potential for fluid in the joint. Scalar waveform features and the computed CID can be used to estimate which joints may contain fluid thereby providing insights into which joint sealant sections may need to be repaired or when a sufficient number of joints may contain fluid suggesting a larger joint maintenance effort be performed to seal the joints or the concrete.

17. Key Words concrete, deicer solutions, freeze-thaw damage, pavement, joints, GPR, resistivity	**18. Distribution Statement** No restrictions. This document is available to the public through the Joint Transportation Research Program, West Lafayette, IN, 47907

19. Security Classif. (of this report) Unclassified	**20. Security Classif. (of this page)** Unclassified	**21. No. of Pages** 39	**22. Price**

Form DOT F 1700.7 (8-69)

EXECUTIVE SUMMARY

EARLY DETECTION OF JOINT DISTRESS IN PORTLAND CEMENT CONCRETE PAVEMENTS

Introduction

Midwestern states have observed premature joint deterioration in jointed plain concrete pavements. It has been proposed that this deterioration occurs when the joint sealants fail, allowing fluid to collect in the saw-cut joint. Problems of joint deterioration (caused by water ingress, freezing, and/or salt reaction) have emerged that can shorten the life of the pavement, requiring expensive and invasive repairs. To effectively apply low cost corrective actions early, detection of fluid in the joints is needed. Concrete pavements can be expected to provide a relatively long service life. This project investigated the use of electrical resistivity and ground penetrating radar (GPR) as two techniques to detect premature joint deterioration.

Findings

The electrical response was measured for mortars subjected to a temperature cycle from 23°C to -35°C with varying degrees of saturation and varying salt concentrations. The resistivity increased as the degree of saturation was reduced due to the reduction in the volume of the conductive medium and increase in tortuosity. The resistivity decreased as the concentration of NaCl increased due to the increased ionic concentration. The resistivity gradually increased as temperature was decreased until the phase transformation temperature (i.e., ice formation), after which time the resistance increased more rapidly. The increase in resistivity can be described using an Arrhenius law for conduction from 23°C due to the phase transformation temperature; however, at temperatures lower than the phase transition temperature, the responses are more complex due to a reduction in conducting fluid and a change in solution concentration. The influence of the degree of saturation and salt concentration on the amount of activation energy seemed relatively small. Changes in resistivity were detected when cracking occurred in the sample, and the magnitude of these changes was similar to that detected using changes in the ultrasonic wave speed.

GPR was used effectively to detect fluid accumulation in the saw-cut joint behind the joint sealant. The typical GPR waveforms are difficult and time consuming to interpret. Features of the wave form (amplitude and derivative) indicate the presence of fluid; however, the XX antenna configuration with the 400 MHz antennas was the most promising due to proportionality with the fluid present in the joint. A signal processing approach termed the complexity-invariance distance (CID) approach, was used to obtain a single number that reflects the potential for fluid in the joint. Scalar waveform features and the computed CID can be used to estimate which joints may contain fluid, thereby providing insights into which joint sealant sections may need to be repaired or when a sufficient number of joints may contain fluid, which suggests that a larger joint maintenance effort be performed to seal the joints or the concrete.

Implementation

Ground penetrating radar is the most promising method that can be used to gain a general understanding of the fluid level in the joint without requiring the removal of the backer rod and silicone sealant. Currently, this process provides only a binary solution to identify whether or not fluid exists in a joint beyond a certain depth. However, refinement of the process and a statistical analysis of the differences between maximum amplitudes of regular and cross polarized scans on a variety of pavements could provide the ability to determine the depth of fluid in a joint.

Direct measurement of electrical resistivity of the concrete from the surface can also be used to identify whether fluid exists in a joint beyond a threshold determined to be indicative of susceptibility to joint deterioration. Like the GPR process, this method will be influenced by many factors independent to each specific pavement. However, this method is not recommended for use in the field due to the increased time required for performing the test.

When joints contain fluid, the potential for joint deterioration occurs. In cases in which fluid is identified, we recommend that a larger investigation be performed to determine the extent of the damage and whether a larger maintenance effort is needed to reseal the joints or the concrete.

CONTENTS

LIST OF TABLES

LIST OF FIGURES

1. INTRODUCTION

1.1 Motivation

INDOT (as well as several surrounding states) have observed that certain concrete pavements may show a susceptibility to joint deterioration. Unfortunately, by the time that this joint deterioration is observed it is often too late and costly partial depth repairs are needed. The deterioration is generally occurring in the joint behind the backer rod and joint sealant; as such, it is difficult to detect even if one is standing directly above the joint. This project evaluated the use of two non-destructive test methods to detect water trapped in pavement joints. The thought process was that if water in the joint is determined at an early stage, low cost corrective actions can be taken to extend the life of the concrete.

1.2 Objectives of Research

This project investigated the identification, evaluation and development of two non-destructive test methods that can be used to determine the level of damage that exists in D-1 pavement joints. The techniques (electrical measurement and ground penetrating radar) were intended to be one sided and able to be performed without the removal of the sealant or backer rod. The goal was to provide an indication of whether damage is developing before it becomes visible at which time the cost of repair is exceptionally high.

1.3 Scope of Work

INDOT has observed that some concrete pavements show premature joint deterioration (Figure 1.1). Unfortunately, by the time that this joint deterioration is observed it is often too late and costly partial depth repairs are needed.

Recent research has shown that damage and repair costs can be greatly reduced if the damage is detected early enough so that the joint can be treated. Unfortunately the deterioration is generally occurring in the joint behind the backer rod and sealant as such it is difficult to detect even if one is standing directly above the joint. This project examined the use of two non-destructive test methods to detect the extent of damage that has occurred in the pavement joint. If the joint is determined to be deteriorating corrective actions can be taken to extend the life of the concrete.

Figure 1.1 Photograph of field observation showing damage in pavement joints.

This joint deterioration is problematic since it compromises the performance and potential service life of an otherwise healthy pavement. If this premature damage can be detected it can provide substantial savings to the citizens of Indiana. Ultrasonic wave speed was investigated; however, the time spent coupling the sensors to the surface suggested that this would be too time consuming and was removed from consideration early in the process. Similarly, thermal imaging was removed early in the process. More promising methods for damage detection include electrical resistivity and ground penetrating radar as methods to detect standing water which often is observed with this type of distress.

2. SAW-CUT PAVEMENT JOINTS

2.1 INDOT Standard Joint

This work was performed for the Indiana Department of Transportation (INDOT) where typical D-1 contraction joints are a standard construction practice as shown in Figure 2.1.

The joint consists of an initial cut with a 1/8″ (3.18 mm) wide blade, down to a depth of one third of the overall depth of the pavement (D/3). This is followed by a second cut that is 1/4″ (6.35 mm) wide to a depth of 1-1/4″ (31.75 mm). The intent of this second cut is to create an opening at the top of the joint, after the crack has occurred, of relatively consistent width to allow for current joint sealing practices. This consists of placing a foam backer rod into the opening to create a backstop for self-leveling silicone joint sealant that will be placed on top. The backer rod should be placed at a depth such that it allows for 1/4″ (6.35 mm) of silicone sealant above the rod, while remaining below the surface in order to minimize mechanical damage from traffic. In an ideal situation saw cutting occurs at an appropriate time after concrete placement, such that the slab has not yet cracked but will crack from the bottom of the saw cut to the drainage layer below the pavement. This allows fluids to escape the joint to the drainage layer, and avoids the fluid retention, which can lead to an increased degree of saturation at the base of the joint or chemical reactions between the deicing chemicals and the concrete. However, for a variety of reasons such as, joint spacing, mixture design, or curing conditions these cracks may not occur in all joints.

2.2 Behavior of a Crack-Free Joint

The susceptibility of a joint to premature deterioration increases dramatically when a crack does not occur to connect it to a drainage layer. Without this escape path, rain water and deicing salts will remain in the joint for extended periods of time, allowing these fluids to be absorbed into the concrete. The relationship between degree of saturation (DOS) and freeze and thaw damage is important. Recently, the work of Li, Pour-Ghaz, Castro, and Weiss (2012) showed that damage will occur

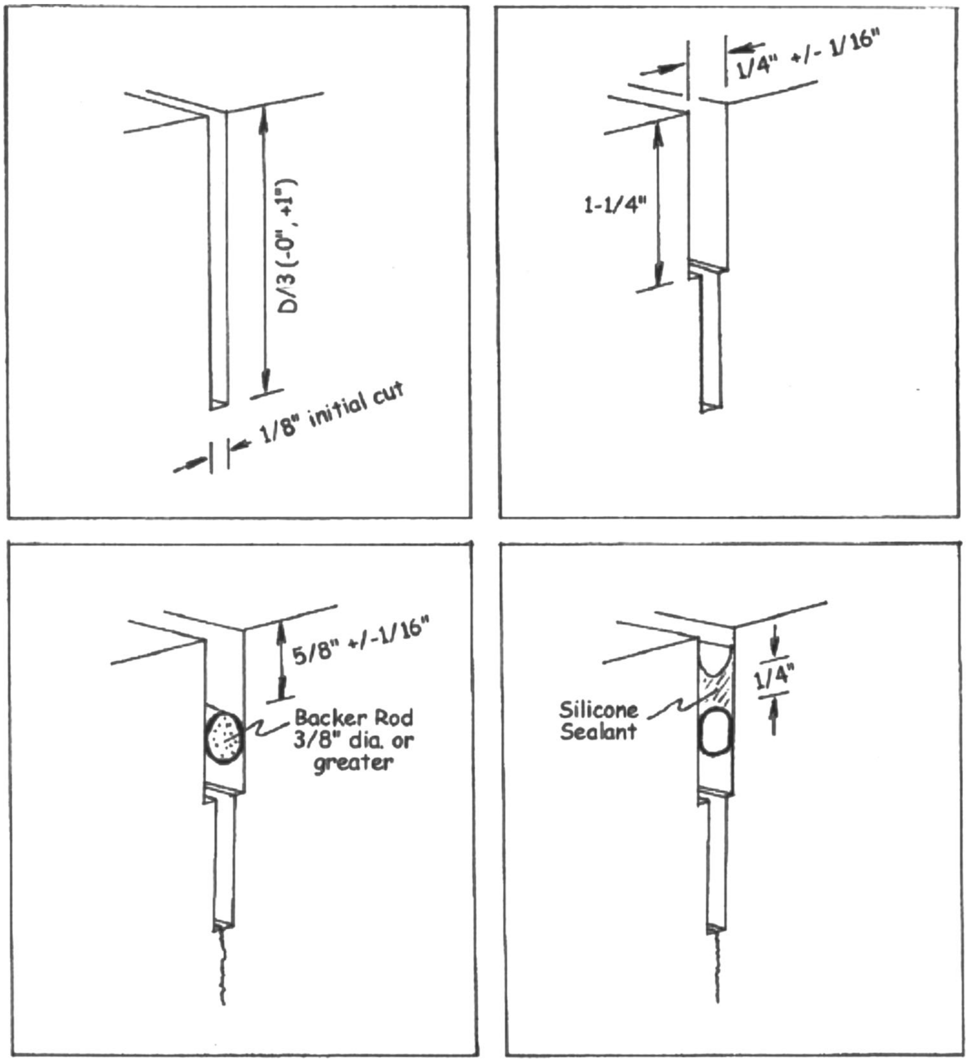

Figure 2.1 Construction of a standard INDOT contraction joint.

when the concrete reaches critical DOS between 86% and 88%, even in just a few freeze and thaw cycles.

2.3 Sealing Methods

The intent of sealing pavement joints is to prevent this type of damage by limiting exposure to fluid. There are two schools of thought when approaching this task. The first is to attempt to limit the amount of fluid that can enter the joint by creating a barrier at the opening of the joint (i.e., a joint sealant). This would be highly effective in theory, but is quite hard to maintain in practice. The second method is to allow water to enter the pavement joint, but prevent it from being absorbed into the concrete (i.e., a concrete sealant). These two methods are illustrated in Figure 2.2.

2.3.1 Joint Sealant

INDOT currently utilizes the first method of joint sealing, preventing water from entering the joint. This could include the use of backer rod and silicone sealant or a hot-pour fill that fills the joint. This method is highly dependent on the concrete and sealing material remaining bonded over time. Further some backer rods are water absorptive which can trap water and accelerate the absorption into the concrete. Over time, even in laboratory conditions, the bond between the sealer and concrete can break down, allowing fluids to pass the barrier and enter the joint. If this occurs what remains of the sealant often blocks sunlight and wind, limiting the evaporation of this fluid. Figure 2.3 shows an example of this condition in joints that have been in an environmental chamber at 23+/-2°C and 50+/-4% relative humidity.

2.3.2 Soy Methyl Ester—Polystyrene Concrete Sealer

The use of Soy Methyl Ester—Polystyrene (SME-PS) sealant is an example of a concrete sealant as shown in Figure 2.2. The work of Golias and Coates Coates, Mohtar, Tao, and Weiss (2009) and Golias et al. (2012)

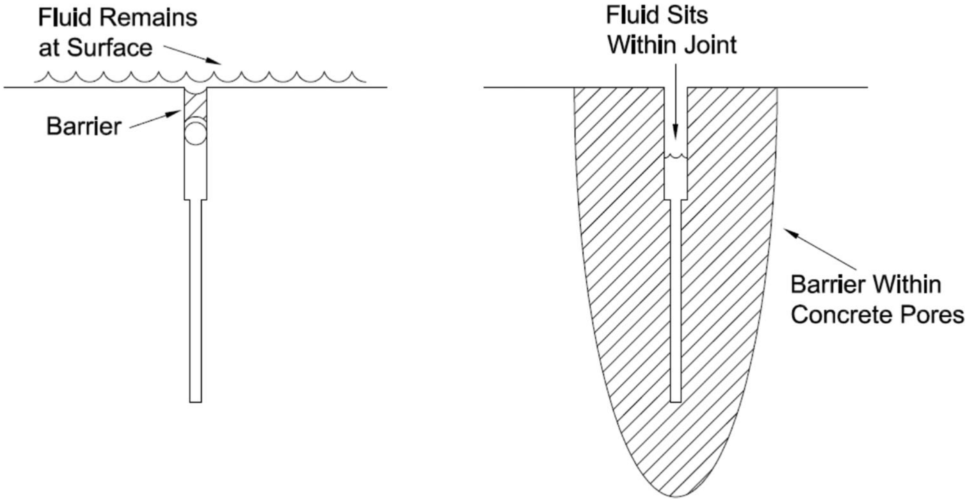

Figure 2.2 Demonstration of different approaches to pavement joint sealing.

has shown that SME-PS can be absorbed into the pore network of the concrete, creating a barrier in the pores. This sealant has been established within laboratory settings as an effective means of reducing fluid ingress. In tests of water absorption, SME-PS reduced absorption by about 72% compared to untreated samples. If this performance can be translated into the field, it will provide an economically feasible approach to the open joint method of sealing.

Figure 2.3 Silicone sealant debonding from concrete at the surface of a joint.

2.3.3 State of Practice and Intention of the Report

Currently the majority of INDOT construction projects specify the use of backer rod and silicone sealant for joint protection. Experience has shown, however, that in some pavements, premature joint deterioration can occur, which becomes a problem. The intent of this report is to provide a method to detect the potential for deterioration before damage becomes evident. These methods are meant to provide an indication what is happening in the joint without requiring the removal of the existing backer rod and silicone sealant. Subsequently, successful field trials of concrete sealer would be able to evaluate whether they provide a potential method for remediation.

3. LABORATORY CONCRETE SLABS

3.1 Overview

The goal of this phase of the project was to investigate the use of electrical measurements and ground penetrating radar to assess fluid in pavement joints, in a controlled, laboratory setting. Concrete slabs were constructed in the laboratory that contained a typical sealing method (backer rod and silicone sealant). Furthermore, the use of a SME-PS sealant was assessed. The slabs, after allowing sufficient curing time were ponded with solutions, either water or calcium chloride ($CaCl_2$). The joints were drained to allow testing of an empty joint, and then the solution level was filled with one, two, or three inches of solution.

3.2 Concrete Slab Materials

Slabs for this study were cast from a ready mixed concrete truck. The concrete mixture was chosen to be similar to a typical INDOT pavement mixture. During the casting the material was consolidated with a vibrator. A summary of this mixture can be seen in Table 3.1. The air content of the concrete (in a fresh

TABLE 3.1
Mixture proportions, in saturated surface dry (SSD) conditions.

Material	Proportion
Cement (lb/yd^3)	658
Water (lb/yd^3)	256
Fine aggregate (lb/yd^3)	1240
Coarse aggregate (lb/yd^3)	1800
Air entraining admixture (fl oz/100 lb cement)	0.6
High range water reducer (fl oz/100 lb cement)	2.00

state) was measured in accordance with ASTM C 231 was found to be 6.2%.

These slabs were cast with a 10″ (25.4 cm) depth, on top of a 1.25″ (3.18 cm) gravel base. Each slab contains two 1″ (2.54 cm) diameter dowel bars centered in the slab, orientated perpendicular to the joint, at a depth of 7″ (17.78 cm) from the pavement surface. Each slab was saw-cut in two stages using a wet saw and diamond blade. First a 1/8″ (0.32 cm) wide cut 4″ (10.16 cm) deep, followed by a 0.25″ (0.64 cm) saw cut 1.25″ (3.18 cm) deep in accordance with INDOT standard practice for concrete pavement joints Indiana Department of Transportation 2011.The only differentiation between the joints in these slabs and joints cut in the field is the time of cutting. In field pavements, cuts must be made at carefully coordinated times in order to keep the pavement from cracking in undesired locations. This is not a concern in these slabs because there are small enough that cracking is not a concern. Instead of being cut 2–12 hours after casting, they were cut 48 hours after casting with the assistance of cutting team from The Concrete Surgeons, based out of Indianapolis, IN. Figures 3.1, 3.2, 3.3, 3.4, and 3.5 show these slabs through each stage of their development.

Figure 3.1 Molds for ten 3′ × 3′ × 10″ slabs.

Figure 3.2 Slab molds, lined with plastic, containing 1.25″ of gravel base and dowel bars.

3.3 Conditioning and Exposure

After casting, these slabs were covered with wet burlap and plastic for 48 hours to promote curing without the loss of moisture. After this period the joints were cut, and then the slabs were placed into an environmental chamber at 23 +/- 2°C (73.4°F) and 50 +/- 4% relative humidity to dry for 30 days. This drying period is meant to open space in the pores in order to leave the concrete vulnerable to the exposure treatments that will follow. The ten slabs were divided into two sets of five; each set was maintained in a similar fashion, with the exception that one set was covered with highly absorbent mats which had been saturated with water. This leaves five slabs with the top surface exposed to drying, and five slabs with a layer of water maintained on the top surface. The intent of this differentiation is

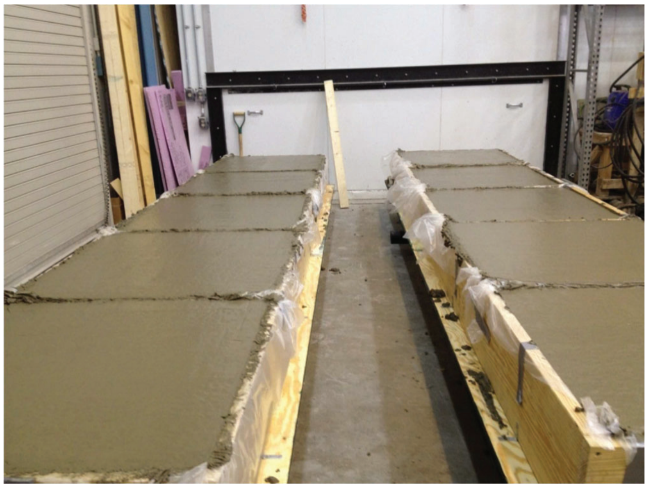

Figure 3.3 Slabs just after casting.

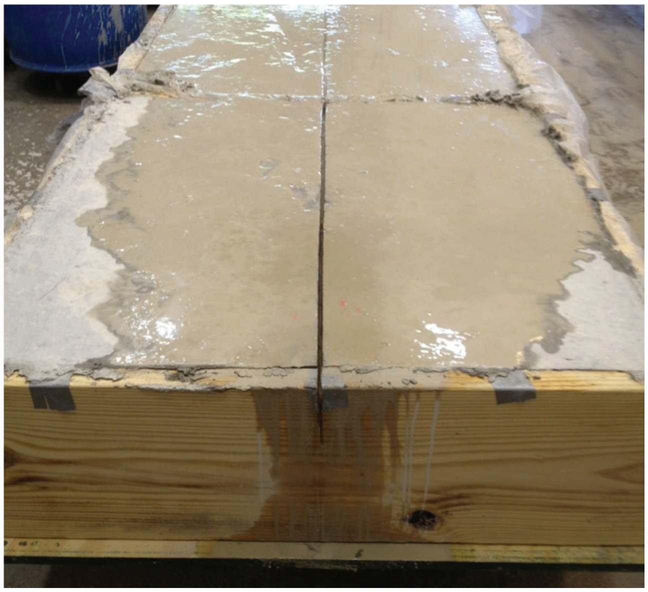

Figure 3.4 Slabs after the saw-cut joints had been made.

to provide a set of dry slabs for a GPR study replicating dry pavements that will be seen in the field, while the other set will maintain a degree of saturation high enough to measure the surface resistivity of the concrete around the joint which will be discussed in Chapter 4.

After the drying period, the slabs were removed from the chamber for sealing. Two of the five slabs in each set were treated with SME-PS in an application manner meant to represent the field application of the product. The ends of the joints were covered an asphaltic adhesive and a border of silicone-rubber sealant. This creates a dam on either end of each slab, leaving a full depth joint through the entire length of the slab that can be filled with fluid from the surface. Each slab, even those treated with SME-PS, was also sealed with the traditional foam backer rod and silicone sealant. This was done to ensure that the condition of the slab matched that seen in the field as closely as possible.

Figure 3.5 Slabs, with molds removed, after curing, and during the drying stage.

Within each set, each of the five slabs was used to mimic a different condition that may be found in pavements that have been in service through real life applications. Of the two that were sealed with SME-PS, one was exposed to water in the joint and the other exposed to 32% (by mass) calcium chloride ($CaCl_2$) in the joint. The remaining three slabs, sealed only with backer rod and silicone sealant, simulate three different conditions. One was exposed to water in the joint, a second was exposed to 16% $CaCl_{2,}$ and the third was exposed to 32% $CaCl_2$. This is meant to demonstrate the capabilities of GPR on pavements that are free of deicing salts, experience a moderate exposure to deicing salts, and see heavy deicing salts respectively. These exposure conditions began within the joint at the end of the 30 day drying period. Joints were filled with solution to the level of the top surface. This level was maintained, beginning with daily refills with the frequency of refills diminishing as absorption slowed.

4. USE OF ELECTRICAL RESISTIVITY TO DETECT JOINT DETERIORATION

Recent techniques for investigating concrete have shown electrical resistivity as a promising nondestructive test method. This chapter evaluates the use of electrical resistivity as a method to detect fluid in the joint in a concrete pavement. It was shown by that when the joint is empty, the current will flow through the concrete around the joint (as air is non-conductive), but when the joint contains fluid the current can flow through the fluid in the joint, and the resistivity will decrease Niemuth, 2004. This suggests that measurements across the joint may provide an indication of whether fluid is in the joint. This method could provide a first estimate as to whether the joint has standing water and the concrete surrounding the joint has a high degree of saturation that would necessitate rehabilitation or a simple fix as a sealant could be applied.

4.1 Electrical Measurements in Concrete

Electrical measurements in porous materials (like concrete) can be described using Equation 4.1:

$$\rho_T = \rho_o \frac{1}{\phi \beta} \tag{4.1}$$

where ρ_T is the total resistivity,ρ_0 is the resistivity of the pore solution which is a function of the ions composition and concentration in solution, ϕ is the porosity of the

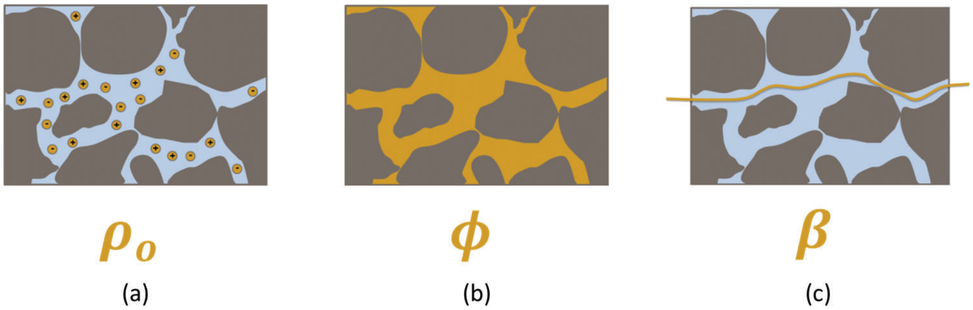

Figure 4.1 Schematic highlighting the parameters used to describe electrical measurements in concrete materials, adapted from Spragg, Villani, et al. (2013).

system that is accessible to fluids, and the β is the connectivity of the pores in the system (Dullien, 1992). A schematic of these different factors is shown in Figure 4.1.

An important parameter to consider in concrete pavements would be the degree of saturation, or what fraction of the porosity ϕ is filled with fluid. At high degrees of saturation, current can easily pass through the concrete and the resistivity is low. At low degrees of saturation, it is difficult for current to flow through the concrete, which results in a high resistivity.

There has been previous research that has studied the impact of the degree of saturation on electrical resistivity measurements (Spragg, 2013; Spragg, Villani, et al., 2013; Weiss, Snyder, Bullard, & Bentz, 2012). These studies have utilized a correction, or a saturation function, that would allow for the resistivity at any level of saturation to be corrected to a comparative measurement at a saturated state (Weiss et al., 2012). This is a power law correction, shown here in Equation 4.2:

$$f(S) = S^m \tag{4.2}$$

where $\boldsymbol{S}$ is the degree of saturation (ranging from 0 at a completely dry state to 1 at full saturation) and $\boldsymbol{m}$ is a fitting coefficient that has been shown to range from 3.0 to 5.0 (Weiss et al., 2012). The fitting parameter has been shown to relate to the connectivity of the fluid phase and pore solution and its ionic strength during drying, and more information is available in the literature (Weiss et al., 2012). This exponent can also be determined experimentally, by saturating a specimen and taking electrical and mass measurements as it dries.

While it is often difficult to determine the degree of saturation of an in-situ pavement or large laboratory specimen, higher degrees of saturation will result in lower values of resistivity.

4.2 Influence of Geometry

Resistivity is material property that is independent of specimen geometry and electrode configuration. However, the *resistivity* is determined from a test of *resistance*. This resistance must be corrected for specimen size and electrode configuration to determine the resistivity. This correction has traditionally been termed the geometry factor, denoted using $\boldsymbol{k}$, and shown in Equation 4.3:

$$\rho = \frac{V}{I} k \tag{4.3}$$

where ρ is the resistivity, $\boldsymbol{V}$ is the measured voltage drop, $\boldsymbol{I}$ is the current, and $\boldsymbol{k}$ is the geometry factor.

One common testing geometry uses an equally-spaced four probe configuration on the surface of a specimen, shown in Figure 4.2. Termed the Wenner test, this test was initially developed for use in soil testing by Frank Wenner at the National Bureau of Standards in the 1910's Wenner 1916. The outer two probes relay a current, while the inner two electrodes will measure the voltage drop.

In the development of the test method, an assumption of an infinite half-space was assumed, that is, the spacing of the electrodes is much smaller (usually by a factor of 6) than the depth of the material being measured ($a << d, L$). If this criterion is satisfied, the geometry factor is given by $\boldsymbol{k}$ in Equation 4.4:

$$k = 2\pi a \tag{4.4}$$

Another common surface test uses four probes, but the spacing is non-uniform. This is termed a Schlumberger array, and is described many places in geophysics literature, (e.g., Keller, 1966), and a schematic is shown in Figure 4.3. The outer two probes relay a current, while the inner two electrodes will measure the voltage drop.

The geometry factor, $\boldsymbol{k}$, for the Schlumberger array is given in Equation 4.5:

$$k = \pi \frac{s^2 - a^2/4}{a} \tag{4.5}$$

where $\boldsymbol{s}$ is the spacing from the centerline of the array to the outer electrodes, and $\boldsymbol{a}$ is the distance between the

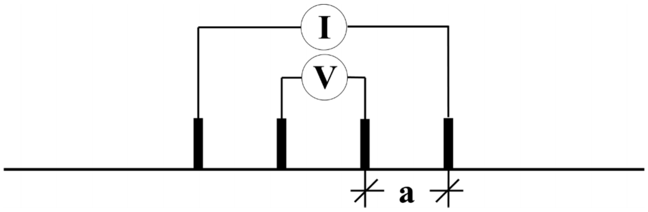

Figure 4.2 Schematic of the Wenner test.

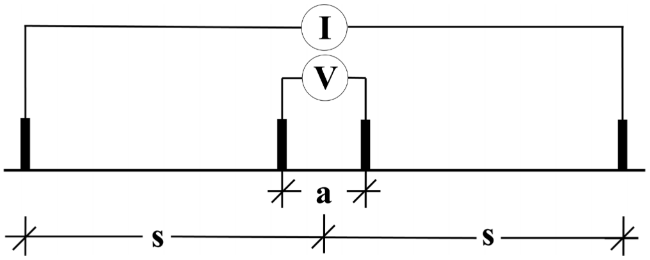

Figure 4.3 Schematic of the Schlumberger test.

two voltage measuring (interior) electrodes. The advantage to using the Schlumberger array is that multiple electrode spacings can be used, as long as a different geometry factor is calculated for each.

4.3 Background on Measurements Conducted on Joints

Changing the spacing of the probes in a surface resistivity test, can be used to amplify or dilute the influence of the joint, shown conceptually in Figure 4.4. For small probe spacings, Figure 4.4a, more of the current is forced to pass through, or go around, an empty joint. If the joint contains conductive fluid it can help to pass current and bridge this gap. For large probe spacings, Figure 4.4b, the current will pass underneath the joint.

A previous study conducted finite element simulations on a jointed slab specimen (Niemuth, 2004). The study investigated plain, un-notched slab specimens, shown in Figure 4.5a. The model also evaluated a notched slab specimen, shown in Figure 4.5b. The results indicate in the presence of a notch, or crack, the distribution of equipotential lines changes.

This study illustrated that electrical measurements were able to determine the location of an empty notch based upon the ratio of resistivity of the material to the measured resistivity (Niemuth, 2004). Furthermore, simulations were conducted that varied the conductivity of the notch, which is equivalent to testing an empty saw cut or a saw cut that

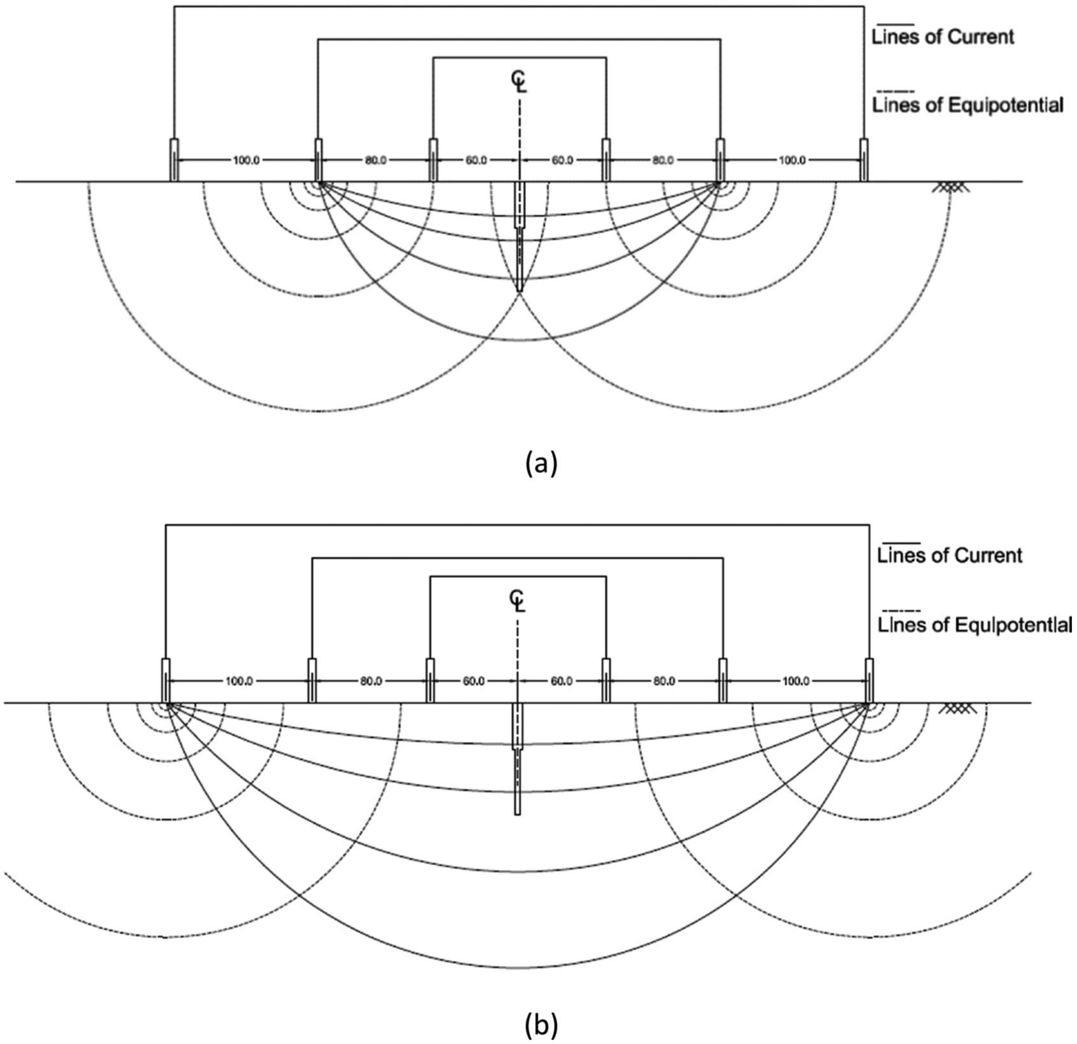

Figure 4.4 Conceptual illustration of a Schlumberger test at (a) close probe spacings and (b) far probe spacings being conducted on a jointed slab.

(a) (b)

Figure 4.5 Heatmap from Finite Element Simulations showing regions of equi-potential conducted on (a) plain slab specimen and (b) notched slab specimen, taken from Niemuth (2004).

has standing water in it. It was determined that closely placed electrodes near an empty notch measured a very high resistivity, whereas a notch filled with conductive fluid was much less resistive than the surrounding concrete, sometimes many orders of magnitude (Niemuth, 2004).

4.4 Experimental Plan for Electrical Measurements on Joints

Five of the slabs used in GPR investigations were maintained under exposure to water from the top surface. This was intended to maintain the degree of saturation at as high a level as possible in the area where measurements were to be taken. Exposure and testing was conducted in a controlled environment of 23 +/− 2°C (73.4°F) and 50 +/− 4% RH. Electrical measurements are very sensitive to temperature changes, so it was important that testing be conducted in a controlled temperature environment.

The five slabs that were measured are identified in results by a slab ID. The ID and sealed and ponding conditions of each slab are listed in Table 4.1.

A testing device, shown in Figure 4.6, was constructed to maintain consistency in electrode spacing and orientation. This was constructed so that electrodes are spaced at 60 mm, 140 mm, and 240 mm from the centerline of the array. The device was manufactured such that it could rotate, and measurements could be taken perpendicular (i.e., 90°) and with a 30° and 60° offset from the axis of the joint, as shown in Figure 4.6b. The intent of rotating the electrode array with respect to the joint orientation is to increase the effective width of the joint along the path of the current.

Electric current was provided between the exterior electrodes and the potential measured by both the middle (designated E/M) and interior (designated E/I) sets of electrodes. After these measurements, the current was moved to the middle electrode in each half of the array and the potential measured by the interior pair of electrodes (designated M/I).

TABLE 4.1
Slabs descriptions for resistivity measurements.

Slab ID	SME-PS Sealed	Exposure Solution
6	Yes	Water
7	Yes	32% $CaCl_2$
8	No	Water
9	No	16% $CaCl_2$
10	No	32% $CaCl_2$

With the device made to maintain consistent electrode position, the electrical measurements were made with a Proceq Resipod. The Resipod operates at a frequency of 40 Hz, and supplies a current up to 200 μA. Electrical measurements have been shown to have a single operator coefficient of variation of 4.36% (Spragg, Castro, Nantung, Paredes, & Weiss, 2012). This device is built as a uniformly spaced 38 mm Wenner probe, and the calibrated to output the resistivity with the geometry correction discussed in the previous section. This study utilized a Schlumberger array, which necessitated the use of a conversion factor. This has been derived below in Equation 4.6, where ρ_w is resistivity measured from the Wenner probe and is the value displayed on the Proceq Resipod, and ρ_s is the resistivity from the Schlumberger array.

$$\rho_w = 2\pi a_w \left(\frac{V}{I}\right) \tag{4.6a}$$

$$\rho_s = \pi \frac{s^2 - a_s^2/4}{a_s} \left(\frac{V}{I}\right) \tag{4.6b}$$

$$\left(\frac{V}{I}\right) = \frac{\rho_w}{2\pi a_w} \tag{4.6c}$$

$$\frac{\rho_w}{2\pi a_w} = \frac{\rho_s a_s}{\pi\left(s^2 - a_s^2/4\right)} \tag{4.6d}$$

$$\rho_s = \rho_w \cdot \frac{2 a_w a_s}{\left(s^2 - a_s^2/4\right)} \tag{4.6e}$$

where a_w is the Wenner probe spacing (3.8 cm), shown in Figure 4.2, and a_s and s are the spacing of the voltage probes and distance from the centerline of the Schlumberger array and the outside current probe, shown in Figure 4.3.

Five measurements were taken in each condition and location. The highest and lowest value from each set were removed and the remaining three data points were averaged. Resistivity measurements were conducted when the joints were empty, and with a fluid depth of 1″ (25 mm) and 2″ (50 mm) in the joint.

4.5 Experimental Results

Recall that testing condition is labeled with two letters specifying active electrodes (Exterior, Middle, or Interior) followed by a dash and the angle, (θ) of measurement.

Measurements taken on empty joints are shown in Figure 4.7. The specimens were ponded with the noted salt prior to testing, and drained at the time of testing. For electrodes spaced widely from the joint,

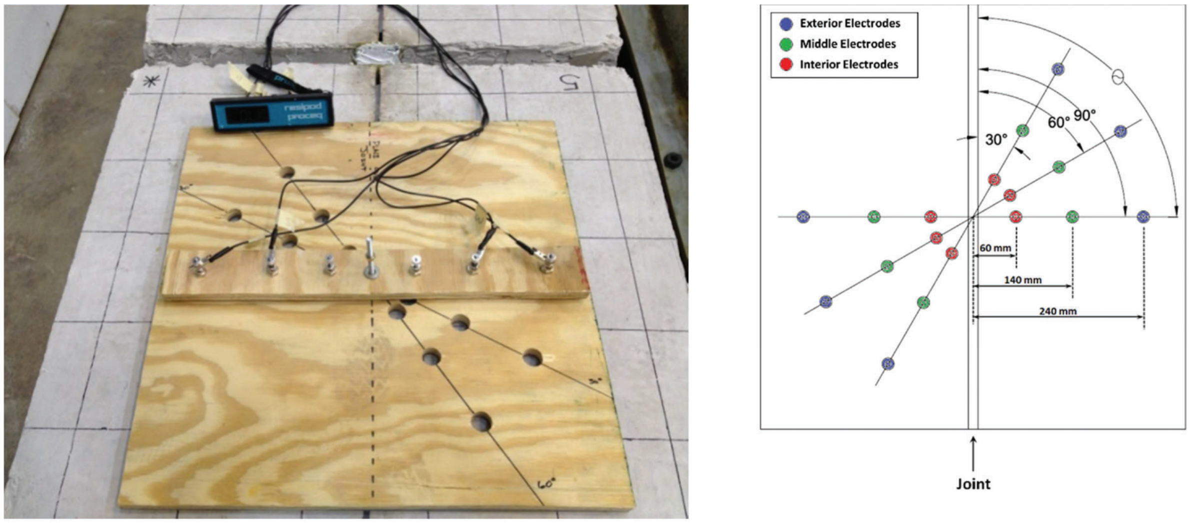

(a)

(b)

Figure 4.6 Electrical resistivity array device developed for this test, (a) shown in a photograph and (b) a schematic that shows spacing, orientation, and nomenclature.

that is, Exterior/Middle (E/M), there is not a significant dependence on probe orientation with respect to joint. This would suggest that far probe spacings probe the material below the joint. Specimens that were sealed with SME-PS before ponding (i.e., slabs 6 and 7) show a sensitivity to electrode orientation at the narrow spacings (i.e., M/I). As the angle with respect to the joint decreases, the effective width of empty joint increases and the resistivity increases as the current is forced to travel around the joint. Lastly, the specimens that were not sealed with SME-PS, ponded with solution, then emptied for initial testing (i.e., slabs 8, 9, and 10) also show to be independent of electrode spacing and orientation. This would suggest that there is a high level of saturation of fluid, especially in the case of slabs 9 and 10 which consist of salt water with low solution resistivity, in the concrete that surrounds the joint. This allows for easy conduction of current around the joint, even when the effective width increases. The higher resistivity of slab 10 (32% $CaCl_2$) compared to slab 9 (16% $CaCl_2$) is a bit surprising because the 32% is much less resistive, but can be explained by much slower fluid absorption of the 32% solution (Spragg et al., 2011).

Figure 4.8 illustrates measurements conducted on jointed slabs that had fluid in the joints. For the widely spaced electrodes (E/M) measurements remained very similar between two and three inches of solution in the joint, and are very similar to the values obtained on empty joints. This confirms that widely spaced probes primarily sample the material below the joint. When using the most narrowly space electrode combination (M/I), a decrease in resistivity is seen with the increasing depth of solution in the joint.

Furthermore, in slabs with fluid in the joints when using narrowly spaced electrodes, increasing the effective width across the joint will actually decreases the resistivity. This is illustrated in Figure 4.8b on slab 10 measurements, where the solid triangle is lower than the hollow triangle. This is contrary to the measurements conducted on dry slabs, illustrated in Figure 4.7, where increasing the effective width across the crack will increase the resistivity. This contrary behavior is one way which can be utilized to assess whether a pavement joint contains standing fluid.

4.6 Summary and Conclusions: Electrical Resistivity for Early Detection of Joint Distress

A procedure for the detection of susceptibility of a joint to premature deterioration was evaluated using measurements of electrical resistivity. The testing configuration consisted of laboratory manufactured Schlumberger array of varying spacing. Measurements were conducted on a Wenner probe, which necessitated the use of conversation factor, which was derived.

It was shown that once accounting for geometry corrections, widely spaced probes can be used to assess the concrete underlying the joint while narrowly spaced probes can be used to assess the joint. The use of narrowly spaced electrodes to assess joint width and potential fluid levels is supported by previous work of Niemuth (2004). Data suggests that electrical measurements conducted on concrete joints that have a high degree of saturation, of which thermal cycling will likely promote joint deterioration, are independent of probe spacing and orientation. This appears a method that shows promise to assess the degree of saturation of concrete surrounding of the joint.

Furthermore, the presence of fluid sitting in a joint, surrounded by concrete with a lower degree of

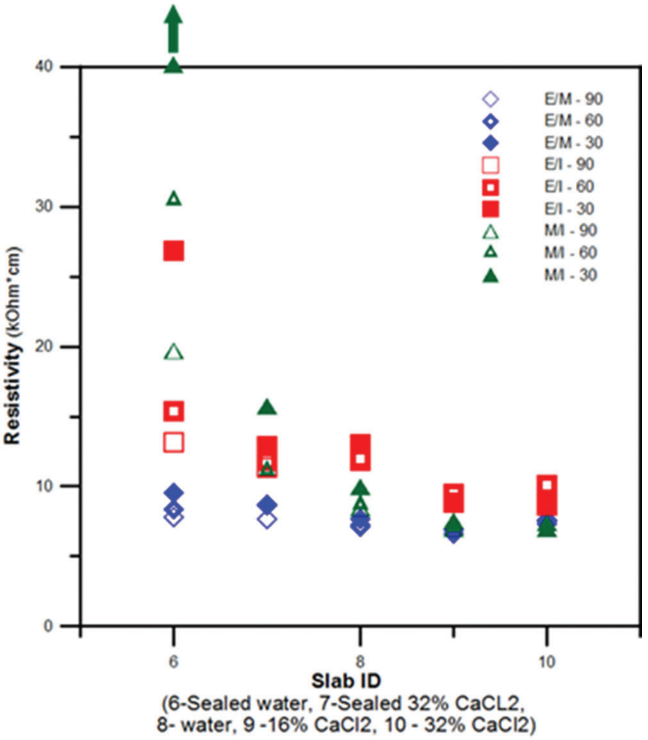

Figure 4.7 Electrical resistivity measurements conducted using the Schlumberger array on empty slab joints. Specimens were ponded with noted solution and drained prior to testing.

saturation, could be accomplished by rotation of narrowly spaced electrode array. Specifically, joints that do not have standing water show a decrease in resistivity as the probe is oriented more perpendicular to the joint, which decreased the effective width of the joint. The presence of solution in the joint manifests itself in the opposite fashion, in which the resistivity will decrease as the probe is oriented more along the axis of the joint. This is attributed the increase in effective width of the joint, which is filled with a solution of lower resistivity than the surrounding concrete. This appears to be an effective method to assess joint drainage. If joint drainage is poor, the concrete surrounding the joint will more quickly reach a critical degree of saturation where thermal cycling will lead to premature deterioration.

While this method appears to have some promise, it can be time consuming compared to GPR, which is discussed in detail in the later chapters of this report. Furthermore, it is worth mentioning that specific values of resistivity are dependent on a large number of factors that are independent to each pavement, including solution in the pores, degree of saturation, and temperature (Spragg, Bu, Snyder, Bentz, & Weiss, 2013; Spragg, Villani, et al., 2013). As such, specific ranges of resistivity values that will lead to premature deterioration are difficult to establish. Instead, the trends discussed above should be assessed. Another potential calibration is normalizing by measurements conducted using widely spaced probes away from a jointed area in an area with well-performing concrete.

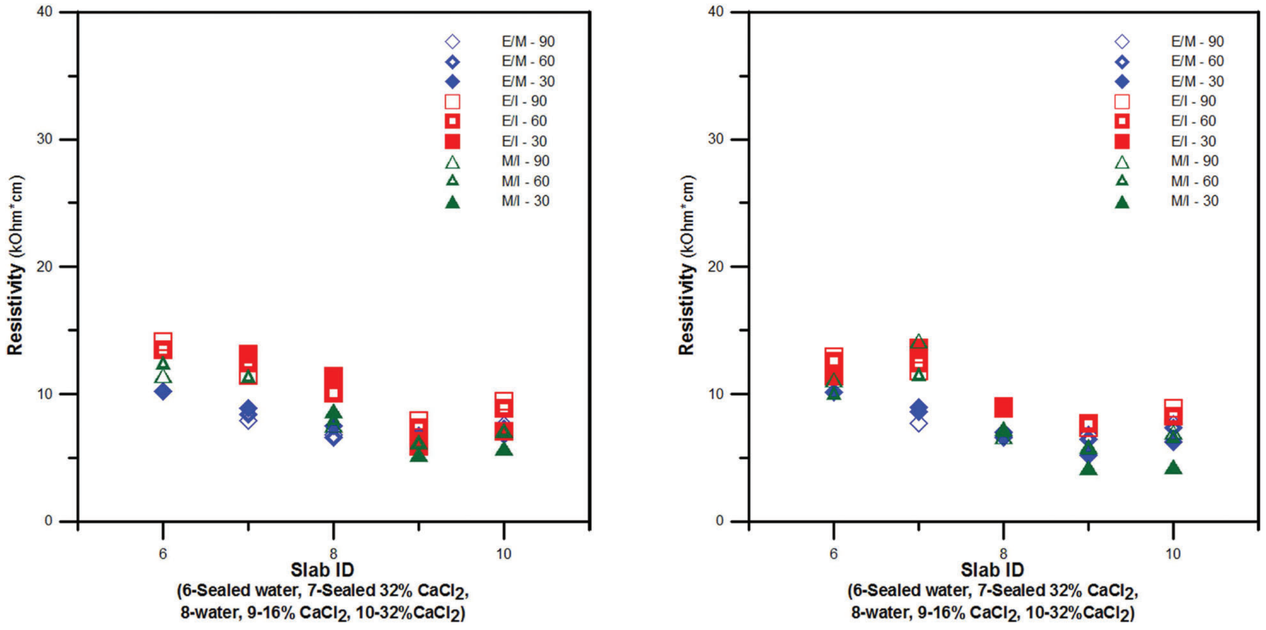

(a) (b)

Figure 4.8 Electrical resistivity measurements conducted using the Schlumberger array on slab joints with (a) 1″ (25 mm) of solution and (b) 2″ (50 mm) of solution.

5. USE OF ELECTRICAL RESISTIVITY TO ASSESS FREEZE-THAW DAMAGE

The electrical testing of cementitious materials is being increasingly performed to assess the quality of concrete. Since its original use by Shimizu in the 1920's (Shimizu, 1928), many researchers have sought to use electrical measurements to describe hydration (Curran & McCarter, 1984; Osterminski, Polder, & Schießl, 2012; Sohn & Mason, 1998; Van Beek & Hilhorst, 1999; Wei & Xiao, 2014), transport properties (Ramezanianpour, Pilvar, Mahdikhani, & Moodi, 2011; Tang, Nilsson, & Basheer, 2011), or cracking (Chung, 2003; Niemuth, 2004; Peled, Torrents, Mason, Shah, & Garboczi, 2001; Pour-Ghaz, 2011; Pour-Ghaz, Niemuth, & Weiss, 2013; Taillet, Lataste, Rivard, & Denis, 2014; Wiwattanachang & Giao, 2011). Electrical testing has many advantages due to the low cost of testing equipment and short time duration that is needed to perform the test. However, the testing geometry (Morris, Moreno, & Sagüés, 1996; Spragg et al., 2012), the testing temperature (Julio-Betancourt & Hooton, 2004; Liu & Presuel-Moreno, 2014; Spragg et al., 2012; Spragg, Villani, et al., 2013), the degree of saturation of the sample (Spragg et al., 2012; Spragg, Villani, et al., 2013; Weiss et al., 2012; Weiss, Shane, Mieses, Mason, & Shah, 1999), and the pore solution concentration/leaching (Castro, Spragg, & Weiss, 2012; Spragg et al., 2012; Spragg, Villani, et al., 2013) must be considered in order to properly interpret the results. While the influence of many of these variables can be minimized through standardization, it is crucial that they are properly considered for.

Many times electrical properties are used to measure the transport properties of concrete, such as the Rapid Chloride Penetrability Test ASTM, 2012a. While several researchers have done excellent work describing changes in the electrical response that occur due to heating (Julio-Betancourt & Hooton, 2004; McCarter, Forde, Whittington, & Ravindrarajan, 1982; Whittington, McCarter, & Forde, 1981) or environmental temperature fluctuations (Nokken, Boddy, Wu, & Hooton, 2008; Sant, Rajabipour, & Weiss, 2008; Spragg, Villani, et al., 2013; Villagrán Zaccardi, Fullea García, Huélamo, & Di Maio, 2009), a relatively small number of researchers have used electrical properties to study freezing concrete (Cao & Chung, 2002). Olson et al. (1995) used freezing to develop a measure of conduction through the capillary and gel pores for to better understand the structure of cement paste. Sato and Beaudoin (2003) examined the freezing behavior of a Wollastonite micro-fiber reinforced cement paste by using an AC impedance spectroscopy.

Previous freeze-thaw studies (Fagerlund, 1975; Li et al., 2012) have shown that the level of damage that develops depends on the degree of saturation (the volume ratio of fluid in the sample as compared to the total volume of fluid that the sample can hold at 7 torr) in a concrete element. It has been suggested that there is a critical degree of saturation (between 80% and 91%) above which freeze-thaw damage can begin to initiate.

Figure 5.1a (Li et al., 2012) illustrates that as the degree of saturation decreases, the level of damage that develops also reduces until the critical degree of saturation is reached. For samples in which the degree of saturation is below the critical degree of saturation, freeze-thaw damage is expected to not occur.

Deicing chemicals can also increase the freeze-thaw damage in concrete by resulting in additional distress due to the osmotic pressure and/or the crystallization pressure (Litvan, 1976; Qian, Farnam, & Weiss, 2014; Scherer, 1999; Shi, Fay, Peterson, Yang, 2010; Valenza & Scherer 2005). Previous studies (Farnam, Bentz, Hampton, & Weiss, 2014; Farnam, Bentz, Sakulich, Flynn, & Weiss, 2014; Farnam, Dick, et al., 2014; Villani, Farnam, Washington, Jain, & Weiss, in press) identified that chemical reactions between the cementitious matrix and salt solution can result in a chemical phase change that can cause severe damage in cementitious materials. Figure 5.1b illustrates the phase diagram for a NaCl-H_2O solution.

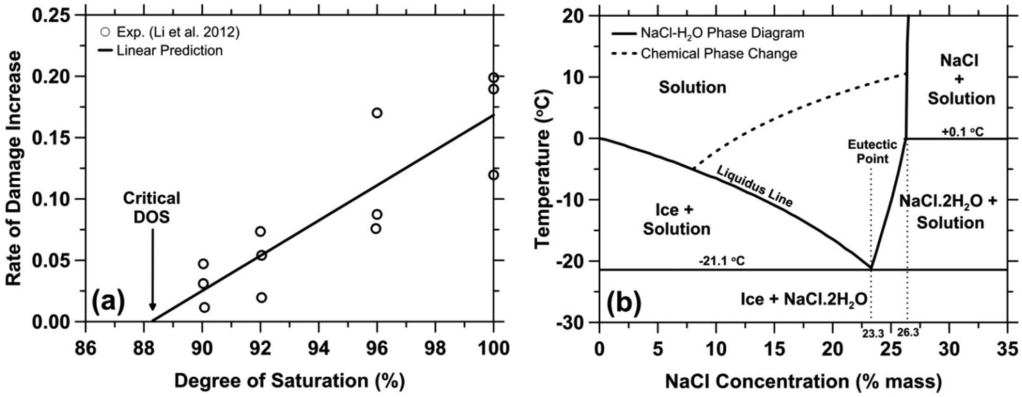

Figure 5.1 (a) Rate of decrease of relative dynamic elastic modulus (freeze-thaw damage) as a function of the degree of saturation (Li et al., 2012) and (b) comparison of NaCl-H_2O phase diagram with chemical phase transition in NaCl-H_2O-cement system (Farnam, Bentz, Hampton, et al., 2014).

Figure 5.1b shows that in a cementitious systems exposed to NaCl, a chemical phase change can occur (as indicated by a dashed line), which was observed at a temperature range between -6°C and 8°C due to the presence of aluminate phases in cement. This chemical phase transition was detected using thermal measurement by observing the heat released during phase transition and the damage was assessed using acoustic emission technique (Farnam, Bentz, Hampton, et al., 2014; Farnam, Bentz, Sakulich, et al., 2014).

Previous research by Olson et al. (1995) examined how the electrical response of a cement paste changed during freezing. This chapter (Farnam, Todak, Spragg, & Weiss, 2015) builds on that work by examining the electrical response of cementitious mortar with varying degrees of saturation and varying NaCl deicing salt concentrations. The main objective of this chapter is to determine whether the electrical resistivity measurement can be used to detect phase changes and to evaluate the damage in mortar samples during freezing and thawing. The effect of the degree of saturation and NaCl deicing salt concentration on the electrical response of the mortar are also studied.

5.1 Experimental Procedures

This section describes experiments performed on two series of mortars that investigated: (1) the role of the degree of saturation (DOS) and (2) the role of deicing salt solutions. The following section describes the sample preparation, sample conditioning, and basic material properties for the two testing series. The second section describes the experimental testing program including the freeze-thaw device (i.e., the longitudinal guarded comparative calorimeter) and the four measurements made on the mortar for all freeze-thaw tests: (1) electrical impedance spectroscopy during freezing and thawing, (2) passive acoustic emission (AE) during freezing and thawing, (3) ultrasonic pulse velocity before and after test, and (4) thermal analysis.

5.1.1 Sample Preparation, Conditioning, and Properties

All tests were performed on a mortar mixture with a water-to-cement ratio (*w/c)* of 0.42 by mass and a sand volume fraction of 55%. The mortar contained ordinary Type I Portland cement (OPC) with a fineness of 375 m^2/kg (C_3S = 60%, C_2S = 10%, C_3A = 9%, C_4AF = 10%, and Na_2O(Equiv) = 0.86%). The aggregate was natural sand with a maximum size of 4.75 mm, specific gravity of 2.61, fineness modulus of 2.89, and an absorption value of 2.2% by mass. ASTM C305-12 ASTM, 2012b was followed during the preparation of the samples in a standard mortar mixer. The mortar samples with dimensions of 25.4 mm × 25.4 mm × 300 mm (1 in × 1 in × 11.81 in) were cast, vibrated, screeded and sealed to cure for 28 d. Following curing, the mortar was cut to 25.4 mm × 25.4 mm × 50.8 mm (1 in × 1 in × 2 in) samples using a wet saw. Samples were then placed in a vacuum oven at 65°C ± 1°C and a pressure of 20 mm Hg ± 5 mm Hg for 7 d to remove their moisture. Upon testing, the samples were individually equipped with wires for EIS testing. The wires were affixed to the top and bottom surfaces of the sample when positioned with the longest side vertical, as they appear in the test setup (Figure 5.2a). A conductive liquid nickel coating was used to hold each separated wire strand on the cross section surfaces and it was assured that the conductive coating covered the entire top and bottom surfaces.

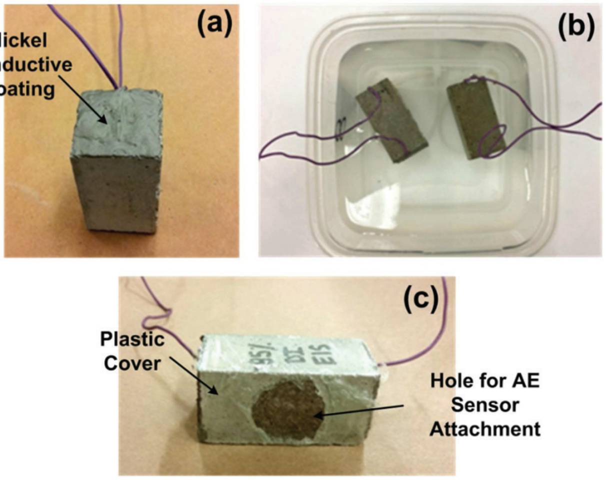

Figure 5.2 (a) Installment of EIS wires using a conductive liquid nickel coating on both sides of the sample, (b) immersion of the sample in the solution to reach saturation before freeze-thaw test, (c) covering the sample with a plastic wrap to minimize the moisture loss during freeze-thaw test, (d) freeze-thaw test setup.

The sample with attached wires was then placed in a desiccator using two small spacers underneath each sample to provide a small gap between the bottom of the container and the lower surface of the sample (Figure 5.2b). The sample was then evacuated to a pressure of 10 mm Hg ± 5 mm Hg for 3 h. While still under vacuum, de-aerated solution (de-aerated by vacuuming the solution for 15 min) was added to the container until the sample was completely submerged and the sample remained submerged in the designated solution under vacuum for 1 h. Afterwards, the submerged sample in the solution was transferred to a 23°C ± 0.5°C chamber and remained in the chamber before testing, approximately 3 d. This condition was considered to be 100% degree of saturation. The deionized (DI) water and NaCl solution (5%, 15%, or 23.3% salt concentration by mass) was used to saturate the mortar samples.

The samples intended for testing at lower degrees of saturation were submerged for 3 d and were then removed from the solution. The samples were allowed to dry and the mass was monitored every 15–30 min until the desired mass (i.e., degree of saturation) was obtained. Samples were then sealed in a double sealed bag for a week before freeze-thaw testing to assure uniform distribution of moisture throughout the sample. Samples with various degrees of saturation (75%, 85%, 95%, and 100%) were prepared. The degree of saturation was determined using the ratio of the volume of absorbed water to the total volume of water that can be absorbed by the sample.

After conditioning and before the freeze-thaw experiment, all sides of the sample not covered in nickel coating were wiped dry and wrapped in a thin plastic layer to prevent moisture exchange with their surrounding environment. A small circular hole was made in one side of the plastic to attach the AE sensor on the surface of the sample to monitor AE activity during freezing and thawing (Figure 5.2c).

Since the conductive coating created uneven top and bottom surfaces, separate samples without coating were prepared for every sample conditioning to perform ultrasonic pulse velocity measurement through the length of the mortar sample before and after freeze-thaw test.

5.1.2 Freeze-Thaw Experimental Testing Program

A freeze-thaw test was performed on a sample conditioned as either: (1) fully saturated (100% DOS) in DI water or NaCl solutions (5%, 15%, or 23.3% concentration by mass), or (2) partially saturated in DI water at various degrees of saturation (75%, 85%, 95%, and 100%). A low-temperature longitudinal guarded comparative calorimeter (LGCC) equipped with continuous passive AE detection and electrical impedance spectroscopy (EIS) was used to investigate electrical response, thermal response, and damage development. A single cooling and heating cycle was used, which varied between 23°C and -35°C with a cooling rate of 2°C/h and a heating rate of 4°C/h. With this setup, one-dimensional heat flow was produced by using a heat sink and an insulated longitudinal guarded aluminum enclosure. Two samples of known thermal properties (Pyroceram Code 9606$^{\text{TM}}$) acted as meter bars to comparatively measure the heat flow through the mortar sample with unknown thermal properties. The LGCC (Farnam, Bentz, Sakulich, et al., 2014) is depicted in Figure 5.3 and was constructed according to ASTM E1225-09 (ASTM, 2009b) and ASTM D5470-12 (ASTM, 2012c).

The test specimen was located between two 25.4 mm × 25.4 mm × 25.4 mm (1 in × 1 in × 1 in) Pyroceram Code 9606$^{\text{TM}}$ meter bars. Thermally conductive pads (ThermaCool TC3008$^{\text{TM}}$) with a thickness of 3 mm, and thermal conductivity of 3.0 W/(m·K) were placed at each interface between the cold plate, Pyroceram$^{\text{TM}}$, and mortar. Thermocouples with an accuracy of ±0.1°C were embedded within the thermopads and were used to monitor the temperature at seven different locations throughout the LGCC.

The thermocouples were used to monitor temperature from which heat flow can be calculated and used to detect endothermic and exothermic behaviors due to phase changes in the system. Temperature sampling was performed at a rate of 0.05 kHz during the thermal cycle. Using the known thermal properties of the meter bar, the heat flow through the Pyroceram$^{\text{TM}}$ can be calculated using Equations 5.1 through 5.4. The heat flow through the mortar specimen can then be estimated by Equation 5.4. It should be noted that the heat flow measured by

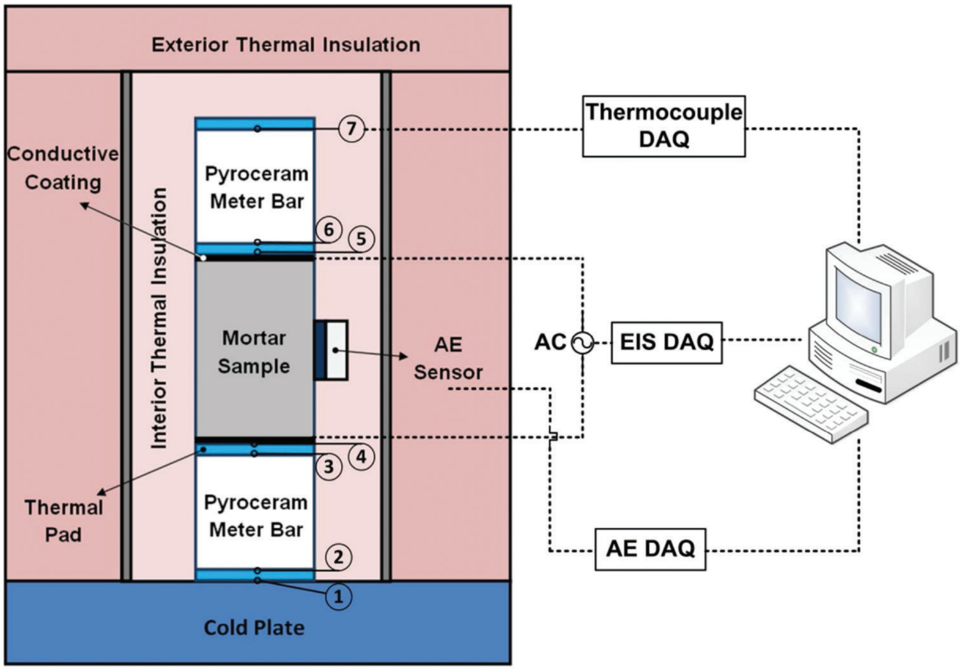

Figure 5.3 Figure illustrating the experimental setup.

this technique is an approximate measurement, since the designed LGCC was operating under quasi-steady state conditions.

$$\lambda_{pc} = -0.0061(T) + 4.2013 \quad -50^{\circ}C < T < 30 \tag{5.1}$$

$$q_T = \lambda_{pc} * \frac{T_6 - T_7}{d_{pc}} \tag{5.2}$$

$$q_T = \lambda_{pc} * \frac{T_6 - T_7}{d_{pc}} \tag{5.3}$$

$$\Delta Q_{Sample} = (q_B - q_T)A \tag{5.4}$$

where λ_{pc} is thermal conductivity (W/(m*K)) of Pyroceram^{TM} at its average temperature, q_T and q_B are respectively heat flow per unit area (W/m^2) through the top and bottom Pyroceram^{TM} meter bars, d_{pc} and A are the thickness of the Pyroceram^{TM} meter bar (m) and the cross- sectional area of the specimen (m^2), respectively, and T_i is the temperature (°C) measured by the thermocouple at location is defined in Figure 5.3.

A single acoustic emission (AE) sensor was embedded into the thermal insulation and held in compression against the surface of the mortar sample. This AE sensor was used in a passive mode to continuously detect AE activity during the thermal cycle (freeze-thaw), that is, detecting the sound waves generated due to cracking in the sample. To measure the compressional wave speed (pulse velocity), similar samples were conditioned without nickel conductive coating and a pulsed wave was generated by using two coupled AE sensors through the length of the specimen before and after the freeze-thaw cycle.

EIS was added to the LGCC to monitor the resistivity of the mortar sample throughout the thermal cycle. This test was conducted with a Solatron 1260A Impedance Analyzer. An alternating current (AC) was applied to the sample with varying frequencies in the range of 0.1 Hz to 10 MHz. This range was intended to provide sufficient data to locate the true resistivity of the sample which occurs at the minimum imaginary impedance. The real impedance which corresponds to the minimum imaginary impedance was multiplied by the geometry factor (i.e., ratio of cross-sectional area to length) to determine the electrical resistivity of the sample, as shown in Equation 5.5. The electrical resistivity measurement of the sample was performed every 3 min (to complete the frequency range) during the thermal cycle.

$$\rho = \frac{A}{L} . R \tag{5.5}$$

where ρ is the electrical resistivity of the sample (Ω.m), A is the cross-sectional area (m^2), L is the length of the sample (m), and R is the real impedance value (Ω) associated to the minimum imaginary impedance.

5.2 Experimental Results

5.2.1 Thermal Response and Acoustic Emission (AE) Activity

During the freeze-thaw cycle, the thermal response of mortar samples was evaluated. Figure 5.4 indicates the temperatures at the top and bottom of the mortar specimen and cold plate for: (a) a mortar partially saturated with water (DOS = 75%), (b) mortar saturated with water (DOS = 100%), (c) a mortar saturated with 5% NaCl by mass (DOS = 100%), (d) a mortar saturated with 15% NaCl by mass (DOS = 100%), and (e) a mortar saturated with 23.3% NaCl by mass (DOS = 100%). In addition, AE activity due to cracking was monitored and is shown in Figure 5.4. The heat flow and cumulative AE signal strength for the mortar samples were calculated and are also plotted in Figure 5.4. The heat flow of the mortar samples can be used to detect phase changes during cooling or heating while the cumulative AE signal strength can be used as an indication for the energy released during cracking (Farnam, Bentz, Sakulich, et al., 2014; Farnam, Geiker, Bentz, & Weiss, 2014).

For samples saturated with water and 5% NaCl solution, one phase change (freezing or melting) was observed due to water/ice phase change. For samples saturated with 15% and 23.3% NaCl, a chemical phase change was also observed in addition to the water/ice phase change. The reaction between cementitious matrix and solutions with higher concentrations (15% and 23.3% NaCl) may result in new chemical products (e.g., Friedel's salt, Kuzel's salt, calcium oxychloride, gypsum, or sodium sulfate) (Farnam, Bentz, Hampton, et al., 2014; Farnam, Bentz, Sakulich, et al., 2014; Farnam, Dick, et al., 2014). The chemical phase change is mainly due to a phase change (from liquid to solid) in the pore solution caused by these chemical products (Figure 5.1b). The chemical phase change during cooling was reported to be destructive and cause damage in cementitious materials (Farnam, Bentz, Hampton, et al., 2014; Farnam, Bentz, Sakulich, et al., 2014; Farnam, Dick, et al., 2014). During freezing, an increase in the temperature and an exothermic behavior (shown by an arrow in this figure) were observed due to latent heat release. During thawing, the specimen temperature remained relatively constant and an endothermic behavior was observed.

5.2.2 Electrical Response

The electrical response for mortar specimens was evaluated during freezing and thawing. The electrical resistivity is plotted as a function of temperature change as shown in Figure 5.5 for samples with different degrees of saturation. As the temperature decreases, an increase in resistivity can be seen due to the temperature effect on electrical resistivity of mortar samples (Nokken et al., 2008; Sant et al., 2008; Spragg, Villani, et al., 2013; Villagrán Zaccardi et al., 2009). As shown in Figure 5.5, a change in the slope of resistivity-temperature curve can be seen as the phase

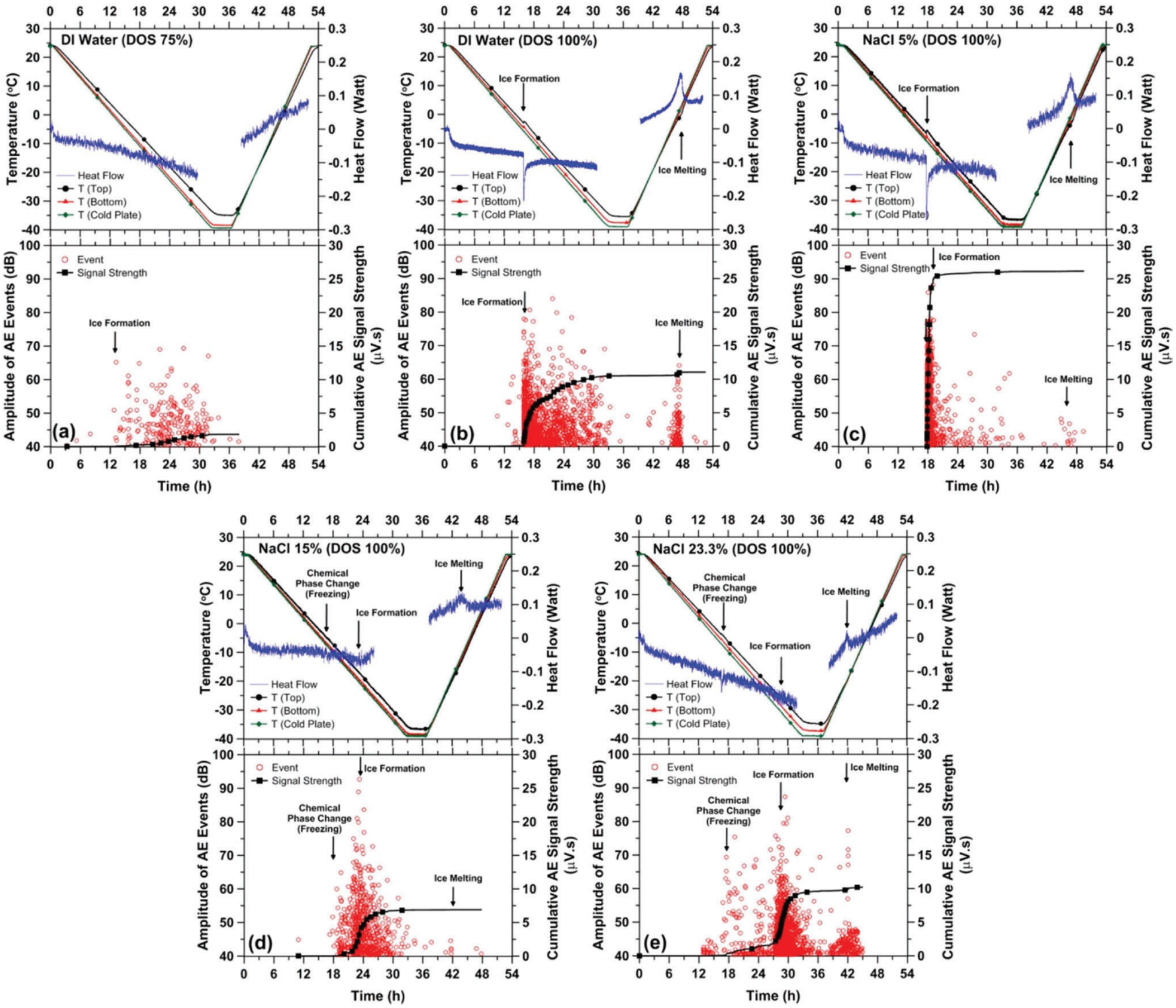

Figure 5.4 Experimental temperature, heat flow and acoustic emission activity for: (a) mortar partially saturated using water (DOS = 75%), (b) mortar saturated using water (DOS = 100%), (c) mortar saturated using 5% NaCl by mass (DOS = 100%), (d) mortar saturated with 15% NaCl by mass (DOS = 100%), and (e) mortar saturated with 23.3% NaCl by mass (DOS = 100%). (Note that the heat flow measurement is not valid between 32 h and 36 h since the sample temperature was kept constant.)

change (i.e., ice formation or ice melting) occurred. This change in slope is mainly due to the change in pore solution conductivity since the conductivity of ice is much less than the conductivity of the pore solution (Cao & Chung, 2002; Olson et al., 1995).

Figure 5.6 indicates the electrical response for mortar samples saturated with solutions containing different concentrations of NaCl. Similar to the DI water saturated samples, changes in the slope of the resistivity-temperature curve were observed during phase changes.

5.2.3 *Effect of Degree of Saturation and NaCl Solution on Electrical Resistivity*

The electrical resistivity in a saturated porous material with a non-conducting solid structure can be described using Equation 5.6 (Dullien, 1992; McCarter et al., 1982; Sohn & Mason, 1998):

$$\rho = \rho_o \frac{1}{\phi\beta} \tag{5.6}$$

where ρ is the resistivity of the porous sample, ρ_0 is the resistivity of the pore solution which is a function of the ionic composition and concentration in solution, φ is the porosity of the system that is accessible to fluids, and β is the connectivity of the pores in the system. The term $\frac{1}{\varphi\beta}$ is often considered as the "formation factor" that is the product of the pore volume and the connectivity (or tortuosity) of the pores in the porous system (Snyder, 2001). Considering the effect of degree of saturation, Equation 5.6 can be rewritten as

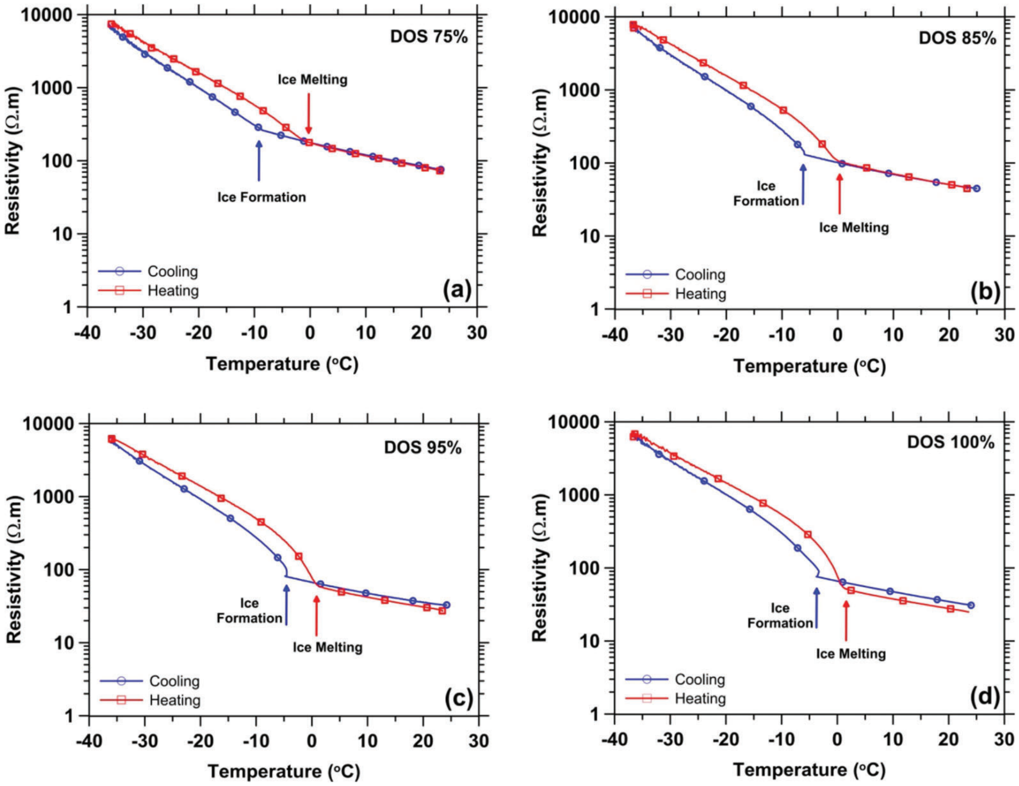

Figure 5.5 Resistivity as a function of temperature for samples with different degrees of saturation.

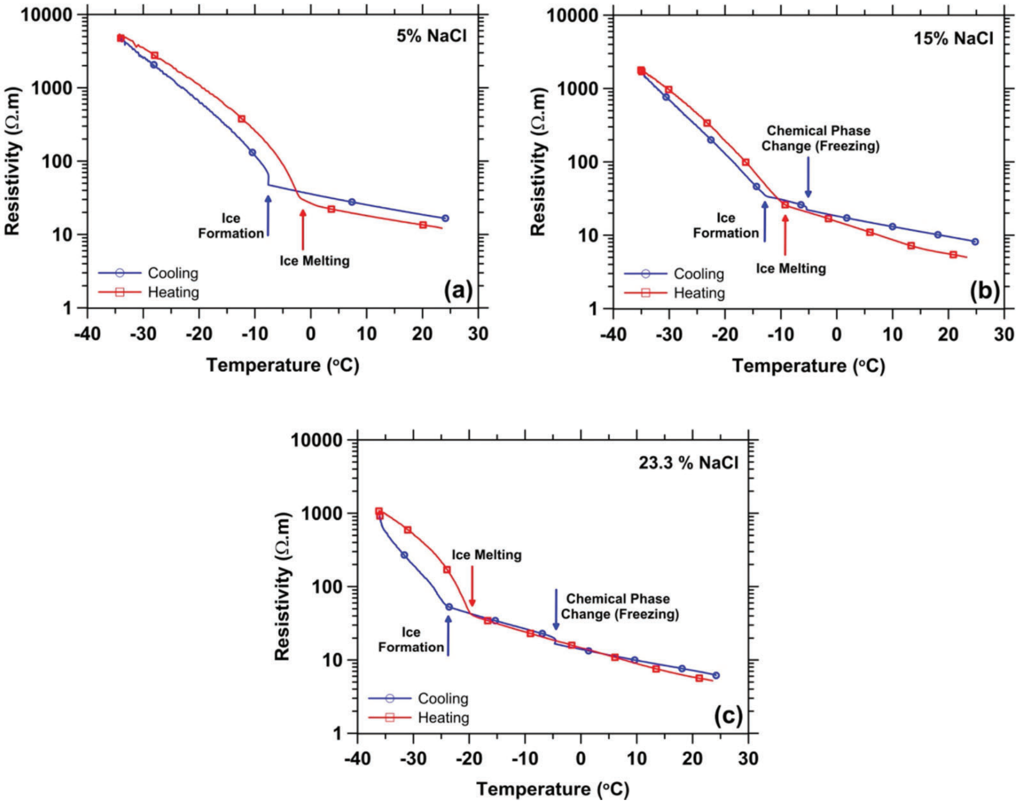

Figure 5.6 Resistivity as a function of temperature for samples saturated with solutions containing different concentrations of NaCl.

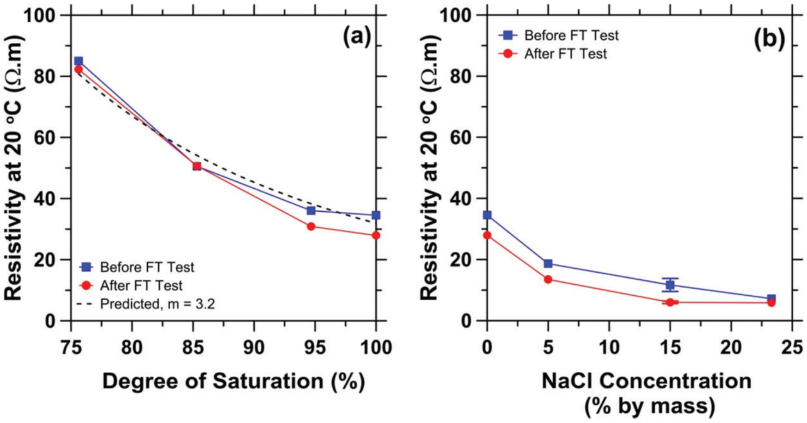

Figure 5.7 Resistivity of mortar samples at 20°C illustrating: (a) the influence of the degree of saturation and (b) the influence of solution concentration.

shown in Equation 5.7 for non–air entrained samples (Spragg, Villani, et al., 2013; Weiss et al., 2012).

$$\rho = \rho_o F \frac{1}{S^m} \qquad (5.7)$$

where ***F*** is the formation factor, ***S*** is the degree of saturation, and is a value between 2 and 5.

The electrical resistivity at 20°C for mortar samples before and after freeze-thaw cycle were detected and are shown in Figure 5.7. As shown in Figure 5.7a, as the degree of saturation for mortar samples decreases, the resistivity of the mortar specimens increases; this is due to the reduction in resistivity of the pore solution (the conductive medium) and increase in tortuosity. A power trendline was fitted to the data point and a value of 3.2 was obtained for. Figure 5.7b shows the effect of NaCl solution on the electrical resistivity of mortar sample. The electrical resistivity becomes lower as the salt concentration increases. In fact, higher amounts of NaCl salt or sodium and chloride ions in the pore solution decrease the pore solution resistivity, ρ_0; as a result, the resistivity of the sample, ρ, decreases.

5.2.4 Activation Energy of Conduction

The temperature of the sample (and pore solution in the sample) can substantially influence the measured resistivity (McCarter et al., 1982; Sant et al., 2008; Spragg et al., 2012; Whittington et al., 1981). An increase in the temperature of the sample results in an increase in the ion mobility in the pore solution and a decrease in measured resistivity. The Arrhenius Law is often used to apply temperature correction shown in Equation 5.8:

$$\frac{\rho_{T_o}}{\rho} = exp\left[\frac{E_a}{R}\left(\frac{1}{T} - \frac{1}{T_o}\right)\right] \qquad (5.8)$$

where ρ_{T_0} (ohm·m) is the resistivity of the sample at a reference temperature, ρ (ohm·m) is the resistivity of the sample at the testing temperature, E_a (kJ/mol) is the parameter known as the activation energy of conduction, is the universal gas constant (8.314 J/(mol·°K)), T(°K) is the testing temperature, and T_0(°K) is the reference temperature (273 K).

The activation energy of conduction (E_a) can be determined using the slope of a plot of the natural logarithm of resistivity and the inverse of temperature multiplied by the negative of the universal gas constant as shown in Equation 5.9:

$$k = -R.\frac{\mathrm{d}(\ln \rho)}{d(\frac{1}{T})} \qquad (5.9)$$

This value was calculated for the EIS results and is shown in Figure 5.8 and Figure 5.9 for the sample saturated with DI water at different degrees of saturation and for sample saturated with NaCl solution, respectively. The value of ***k*** is equal to the activation energy of conduction (E_a) for a wide range of temperature if the pore solution remains at a same phase during temperature change (i.e., no phase changes occur). As phase changes occur, ***k*** is not representative of E_a. The activation energy of conduction was calculated for the mortar samples at 20°C when the pore solution was liquid. The values of E_a are reported in Table 5.1 for the samples saturated with DI water at different degrees of saturation and for the samples saturated with NaCl solution before and after freeze-thaw test. It appears that the influence of the degree of saturation and salt concentration on the amount of activation energy seems relatively small since the average of data points and its variation are relatively near the average and the standard deviation calculated for two samples saturated with 15% NaCl solution (average value = 21.9 kJ/mol, and standard deviation = 1.4).

5.2.5 Detection of Phase Changes Using EIS and Thermal Analysis

Any phase change can substantially alter the electrical response of a porous material. During freezing, a large portion of pore solution transforms to a solid state which cause a large reduction in the volume of pore solution (π). The connectivity of the pore structure (β) also changes

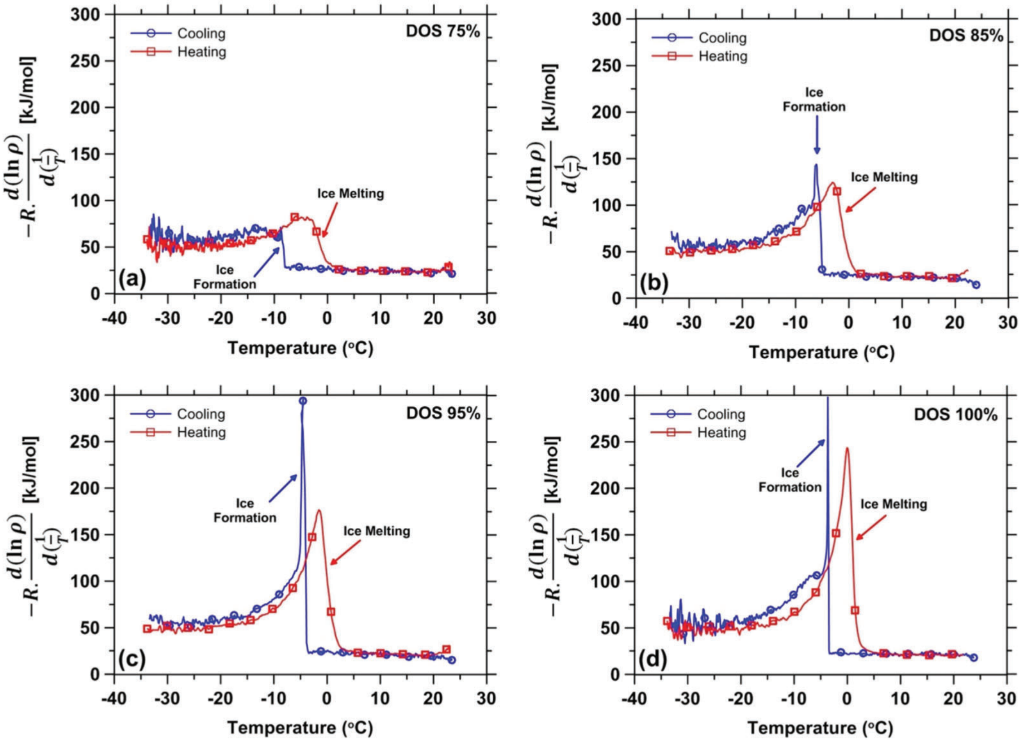

Figure 5.8 Slope of ln(ρ) vs 1/T curve multiplied by the negative of the universal gas constant for samples saturated using DI water at different levels of degree of saturation.

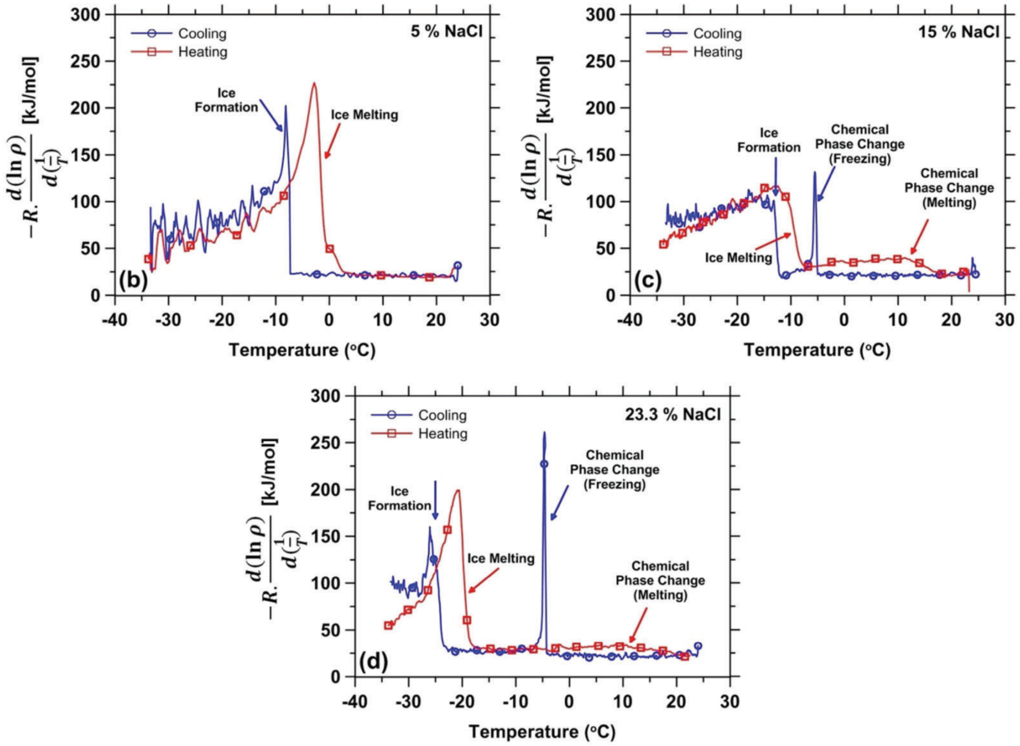

Figure 5.9 Slope of ln(ρ) vs 1/T curve multiplied by the negative of the universal gas constant for samples saturated using solutions with (a) 0% NaCl, (b) 5% NaCl, (c) 15% NaCl, and (d) 23.3% NaCl.

TABLE 5.1
Activation energy calculated for mortar samples before and after freeze-thaw test.

Mortar Samples		Activation Energy at 20°C (kJ/mol) Before Test	After Test
Series I—Degree of Saturation			
75% DOS		22.8	24.1
85% DOS		21.0	22.5
95% DOS		18.8	20.9
100% DOS		21.7	21.1
Series II—NaCl (100% DOS)			
0% NaCl		21.7	21.1
5% NaCl		20.7	19.5
15% NaCl*	Sample 1	24.2	21.1
	Sample 2	21.3	20.9
23.3% NaCl		23.2	23.5
Average		21.6	21.6
Standard Deviation		1.8	1.4

*For 15% NaCl, two samples were tested to define the data variation and uncertainty for EIS measurement.

during ice formation since ice crystals can fill in the pores restricting flow paths or the ice can result in cracking. During freezing, the concentration of the pore solution also varies (as ice forms the pore solution becomes more concentrated following the liquidus line) and this can change the electrical response of the pore solution, that is, ρ_o. The changes in the volume of the pore solution, the connectivity of the pore structure, and the concentration of ions in pore solution can change the electrical response of the mortar samples (see Equation 5.6) (Rajabipour, 2006).

As shown in Figure 5.5 and Figure 5.6, all phase changes caused substantial changes in the slope and the electrical resistivity of the mortar samples. In addition, the slope of $\ln(\rho)$ vs $\frac{1}{T}$ plot multiplied by the negative of the universal gas constant (i.e., $\boldsymbol{k}$ (kJ/mol)), shown in Figure 5.8 and Figure 5.9, has a dramatic increase or decrease during freezing or thawing, respectively. These plots were used alongside heat flow curves (Figure 5.4) to obtain the freezing and thawing temperatures associated with every phase change during freeze-thaw cycle. Table 5.2 reports the freezing and thawing temperatures due to ice/water phase change or the chemical phase transition. Freezing point were detected at a lower temperature than melting point due to the under-cooling effect (Debenedetti & Stanley, 2003). As the degree of saturation decreases, the melting and freezing temperatures decrease due to the fact that the ion concentration (alkali ions from cement) in the pore solution increases at lower degrees of saturations. An increase in ion concentration can depress the freezing point of the pore solution. The chemical phase change was observed in temperatures between -4.5°C and -8°C during freezing and near +10°C during thawing. It should be mentioned that while change in heat flow (LGCC test) was relatively small for freezing or melting of the chemical phase transitions (Figure 5.4), a substantial change in k was observed for this phase change (Figure 5.9). This may show that electrical measurement can be a promising approach to detect phase changes in a porous material.

5.2.6 Evaluation of Freeze-Thaw Damage Using EIS and Acoustic Emission

As shown in Equations 5.6 and 5.7, electrical measurement can be used to evaluate the pore structure of a porous system by determination of the formation factor, F. During freeze-thaw cycle, damage caused by ice

TABLE 5.2
Freezing and melting temperatures associated with phase transitions for mortar samples during freeze-thaw test (the maximum standard deviations for the temperature and resistivity measurements were determined to be ±1.3°C and 2.1 Ω.m, respectively).

Mortar Samples	Expected Freezing Temperature for the Solution (°C)	Freezing Temperature During Cooling (°C)*		Melting Temperature During Heating (°C)*		Resistivity at 20°C (Ω.m)	
		Ice Formation	Chemical Phase	Ice Melting	Chemical Phase	Before Test	After Test
Series I—Degree of Saturation							
75% DOS	0	-9.0	N/A	-2.0	N/A	85.0	82.2
85% DOS	0	-6.5	N/A	-2.5	N/A	50.6	50.7
95% DOS	0	-5.0	N/A	1.0	N/A	36.1	30.9
100% DOS	0	-4.0	N/A	0.5	N/A	34.5	27.9
Series II—NaCl (100% DOS)							
0% NaCl	0	-4.0	N/A	0.5	N/A	34.5	27.9
5% NaCl	-4	-8.5	N/A	-2.0	N/A	18.6	13.5
15%NaCl							
Sample 1	-12	-13.0	-5.5	-9.0	~+10†	9.6	5.6
Sample 2	-12	-11.0	-8.0	-8.0	~+10†	13.8	6.4
23.3% NaCl	-21.1	-24.0	-4.5	-21.0	~+10†	7.2	5.9

*The onset temperature was reported for all phase changes using Figure 5.8 and Figure 5.9.
†Approximate value is reported because it was difficult to find the onset value.

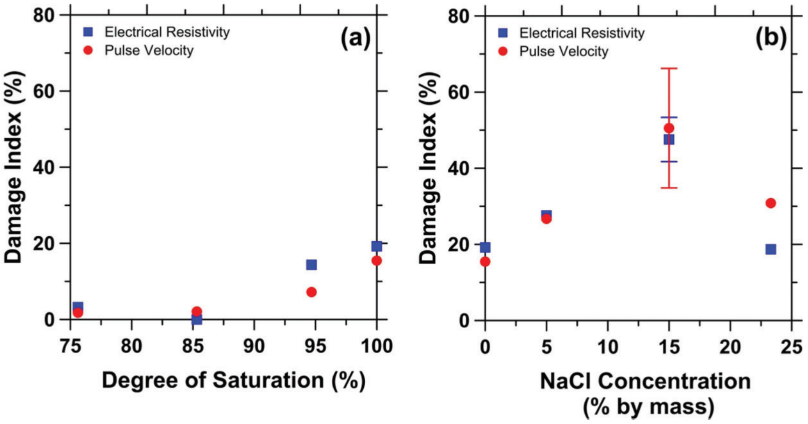

Figure 5.10 Damage index and reduction in resistivity for: (a) samples with different degrees of saturation, and (b) samples saturated with solutions containing different concentrations of NaCl.

formation, osmotic pressure, crystallization, or possible chemical reactions can alter the formation factor resulting in change in the electrical resistivity. Several studies have shown that damage development can be determined by using electrical resistivity measurement and it is related to the fractional change in electrical resistivity of a cementitious material (Cao, Wen, & Chung, 2001; Chung, 2003; Peled et al., 2001; Wen & Chung, 2000, 2007). Assuming no change in the pore solution properties during freeze-thaw, any change or reduction in the electrical resistivity can be representative of change in the pore structure or damage in the system. The change in the electrical resistivity before and after freeze-thaw cycle can be calculated for mortar samples using Equation 5.10 and can be used as a damage index for mortar samples calculated with the electrical resistivity (ER) approach.

$$Damage\ Index\ (ER) = 1 - \frac{F_a}{F_b} = 1 - \frac{\rho_a}{\rho_b} \qquad (5.10)$$

where F_b and F_b are formation factor and resistivity calculated for mortar samples at 20°C, respectively, before a freeze-thaw test; and F_a and ρ_a are formation factor and resistivity calculated for mortar samples at 20°C, respectively, after a freeze-thaw test. The damage index calculated with EIS measurement is indicated in Figure 5.10 and is compared with the damage index calculated with the pulse velocity (PV) approach using Equation 5.11 in accordance with ASTM C597-09 (ASTM, 2009a).

$$Damage\ Index\ (PV) = 1 - \frac{E_a}{E_b} = 1 - (\frac{V_a}{V_b})^2 \qquad (5.11)$$

where E_b and V_b are dynamic elastic modulus and average pulse velocity, respectively, before a freeze-thaw test; and E_a and V_a are the dynamic elastic modulus and average pulse velocity, respectively, after the freeze-thaw test.

Relatively little damage was observed for mortar samples with degrees of saturation equal to 75% and 85% (Figure 5.10a), since the level of saturation for these samples were lower than the critical degree of saturation (between 86% and 88%) to cause freeze-thaw damage for these mixtures (Li et al., 2012). For degrees of saturation more than the critical degree of saturation, damage index increases for both ER and PV approaches as the degree of saturation increases.

Figure 5.10b shows the damage index calculated for samples saturated with solutions containing different concentrations of NaCl. Addition of NaCl to the solution increases freeze-thaw damage in mortar samples. For samples saturated with low salt concentration (0% and 5% NaCl), damage is primarily due to ice formation, in the form of hydraulic pressure and osmotic pressures. Addition of 5% of NaCl to DI water increases the freeze-thaw damage in mortar samples due to additional damage caused by osmotic pressure. Mortar samples exposed to high salt concentrations (15% and 23.3%) shows also considerable freeze-thaw damage; this is due to the damage caused by the combination of ice formation (hydraulic pressure and osmotic pressure) and the chemical phase transition. It should be mentioned that freezing of highly concentrated solution will produce less ice which will likely be not sufficient to cause considerable damage in mortar samples. Therefore, it can be concluded that the chemical phase change (from liquid to solid) in the pore solution during cooling may be the main source of damage in samples saturated with 15% and 23.3% NaCl solutions (Farnam, Bentz, Hampton, et al., 2014; Farnam, Bentz, Sakulich, et al., 2014; Farnam, Dick, et al., 2014).

5.3 Summary and Conclusions

This study has shown the electrical response of mortars subjected to a thermal temperature cycle from 23°C to -35°C. Specifically two series of experiments were performed: (1) mortar with varying degrees of saturation and (2) mortar containing varying concentrations of deicing salt solutions (made using sodium chloride, NaCl). As expected, the resistivity increased as the degree of saturation was reduced due to the reduction in the volume of the conductive medium and increase in tortuosity (Rajabipour, 2006). As expected, a decrease in resistivity was observed as the concentration of NaCl increased due to the increased ionic concentration which facilitates electrical conduction.

As the temperature of the sample was reduced, the resistivity gradually increased until the phase transformation temperature (i.e., ice formation or chemical phase transition) was reached, after which time the resistance increased more rapidly. The increase in resistivity can be described using an Arrhenius law for conduction from 23°C to the phase transformation temperature; however, at temperatures lower than the phase transition temperature, the responses is more complex due to a reduction in conducting fluid and a change in solution concentration. The influence of the degree of saturation and salt concentration on the amount of activation energy seemed relatively small. The phase transition temperature in mortar was lower than that expected during cooling due to under-cooling as a result of difficulties in nucleating ice. In addition, the freezing temperature decreased as the degree of saturation decreased due to the increased ionic concentration (alkalis) in the pore solutions. However, the melting phase transition temperature was what would be expected from the water-NaCl system.

Changes in resistivity were also detected when cracking occurred in the sample due to the freeze-thaw cycle. For mortar samples with the degrees of saturation less than the critical degree of saturation, relatively no damage was observed. The extent of damage that formed began to increase as the degree of saturation increased above the critical point. The addition of NaCl to DI water increased the freeze-thaw damage in mortar samples in comparison to samples saturated with only DI water. For samples saturated with NaCl solutions, two main additional sources of damage can be determined: osmotic pressure and chemical phase transition. The increase in damage at low concentrations (5%) is mainly due to the damage caused by the osmotic pressure in addition to the hydraulic pressure caused by ice formation. For higher concentrations (15% and 23.3%), the high level of damage is due to the chemical phase change in addition to osmotic and hydraulic pressures.

6. USING GROUND PENETRATING RADAR TO DETECT INDICATORS OF PREMATURE JOINT DETERIORATION IN CONCRETE PAVEMENTS

6.1 Introduction and Background

The Indiana Department of Transportation (INDOT) and several other Midwestern state Departments of Transportation (DOTs) have observed that some jointed plain concrete pavements may develop premature joint deterioration (Jones et al., 2013, p. 143; Sutter et al., 2008; Taylor, Sutter, & Weiss, 2012). While the exact causes of this damage are not known it has been reported that fluid ingress at the joints (the fluid being a salt water solution) plays a significant role in the damage (Spragg et al., 2011; Yang, Weiss, & Olek, 2006; Yang, Weiss, Olek, & Nantung, 2005). It has been proposed that the geometry of the saw cut can trap this fluid in the joint leading to a high local degree of saturation (Pour-Ghaz, Rajabipour, Couch, & Weiss, 2009). This high degree of saturation can result in hydraulic and osmotic pressures when ice forms during freezing which can result in cracking of the concrete (Li et al., 2012). As the salt concentration increases chemical reactions can also occur resulting in the form of sodium sulfate (Farnam, Bentz, Hampton, et al., 2014; Farnam, Bentz, Sakulich, et al., 2014; Qian, Farnam, & Weiss, 2013) with sodium chloride, expansive oxychloride when calcium chloride is the deicing salt (Farnam, Dick, et al., 2014; Sutter, Peterson, Touton, Van Dam, & Johnston, 2006) and brucite, magnesium silicate hydrate and oxychloride when magnesium chloride is the deicing salt (Farnam, Dick, et al., 2015; Farnam, Wiese, et al., 2015; Shi et al., 2010; Sutter et al., 2006). Approaches to reduce the potential for damage could include mixture design modifications, joint cross section detail modifications, alternative cements, or methods to reduce water ingress through sealers (Coates et al., 2009; Jones et al., 2013, p. 65). Of these approaches, it is the potential use of concrete sealers which may be the most promising for existing pavements that may show signs of distress; however, this requires that the damage can be detected early. Unfortunately, by the time that this joint deterioration is observed during pavement surface inspection the damage is often extensive which may minimize the potential for topical/penetrating sealers to be used resulting in the need for and costly partial depth repairs.

To understand how this damage forms it is important to understand the geometry of the typical construction joint. The INDOT uses D-1 contraction joints in the longitudinal and transverse joints of jointed plain concrete pavements. The typical joint geometry that will be investigated in this study is shown in Figure 6.1. The D-1 joint is made from an initial cut shortly after the pavement is placed using a 1/8″ (3.18 mm) wide saw blade down to a depth of one third of the overall depth of the pavement (Figure 6.1a). A second cut is made several days later that is approximately 1/4″ (6.35 mm) wide and 1-1/4″ (31.75 mm) deep. The intent of this second cut is to create an opening at the top of the joint for the placement of joint sealer and the delay between the first and second saw cut is to allow the width of the joints to be stabilized (Figure 6.1b). A foam backer rod (a non-absorptive backer rod is preferred) is then placed into the opening to create a backstop for self-leveling silicone joint sealant that will be placed in the joint (Figure 6.1c). The backer rod is placed at a depth such that it allows for 1/4″ (6.35 mm) of silicone sealant above the rod, while remaining below the surface in order to minimize mechanical damage from traffic (Figure 6.1d).

In an ideal situation saw cutting occurs at an appropriate time after concrete placement, such that the slab has not yet cracked or developed a residual stress that is sufficient to cause a crack to develop as the saw cutting

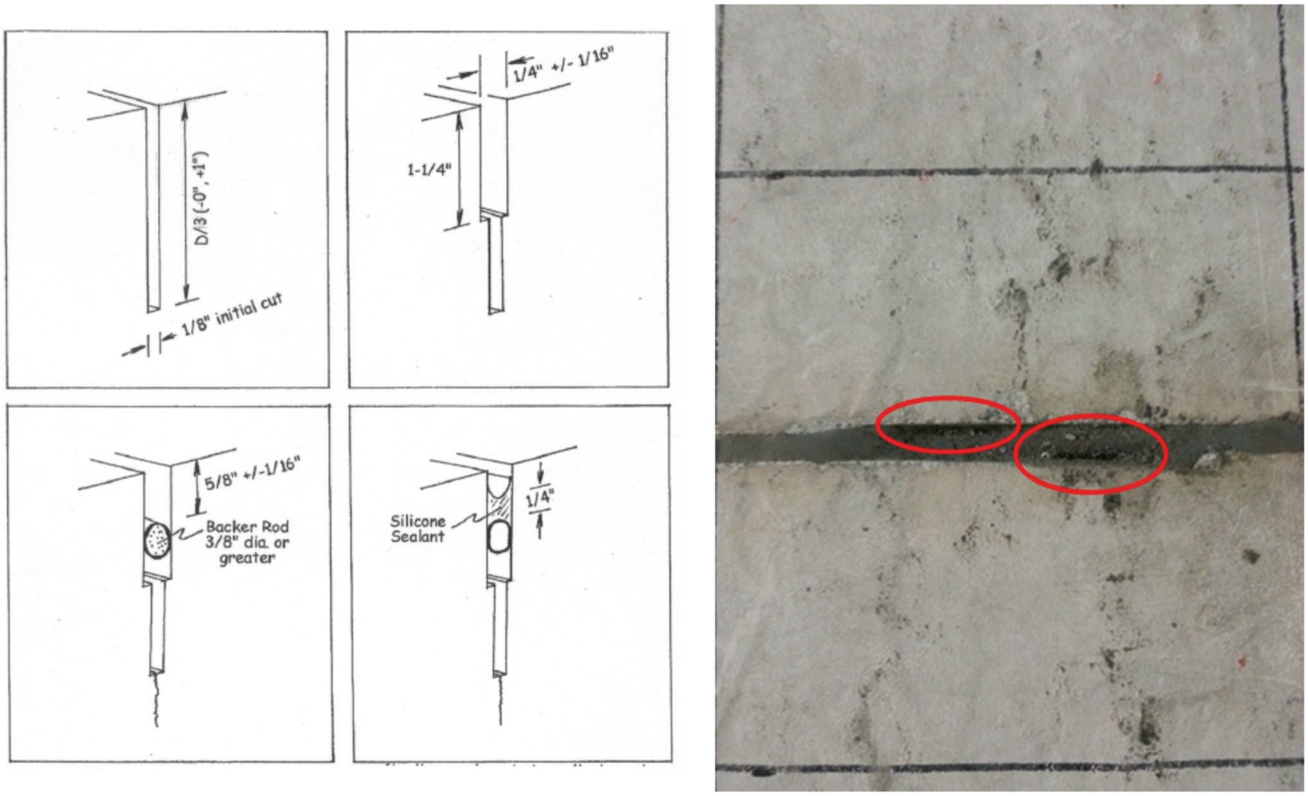

(a) (b)

Figure 6.1 (a) Illustrated construction sequence for a standard INDOT D1 contraction joint and (b) an illustration of a debonding joint sealant.

is being performed (Raoufi, Radlinska, Nantung, & Weiss, 2009). It is anticipated that after the saw cut is placed it will result in a crack that relieves the built in stresses in the pavement. Once the crack forms it is expected that it will extend from the bottom of the saw cut to the drainage layer below the pavement. A properly designed joint anticipates that the joint sealant would remain bonded to both sides of the saw cut after the crack forms thereby keeping fluid and incompressible materials out of the saw-cut joint. However, in many cases this joint sealant may not adhere or may pull away from the concrete allowing fluid to enter the joint (e.g., Figure 6.1b). In joints that have cracked, the crack would allow fluids that may enter the saw cut to be transported to the drainage layer. In joints where the crack does not form, fluid can be retained in the joint which can lead to an increased degree of saturation at the base of the joint and an increase in salt concentration which can lead to deleterious reactions.

While later stages of joint deterioration are quite noticeable with spalling concrete, the failure of the bond between the sealant and concrete is difficult to detect even if one is standing directly above the joint (Figure 6.1b). Having the ability to locate standing fluid in the pavement joints non-destructively would be beneficial indicator for identifying joints susceptible to early deterioration long before this may become visible damage. Early detection of standing fluid in the joints may provide DOTs with an opportunity to replace the joint sealants or to apply concrete sealants to extend the life of the concrete before the joint damage reaches a level where partial depth repair is needed.

This research project examined the potential use of ground penetrating radar (GPR) for locating fluid in the joints in jointed plain concrete pavements (JPCP). GPR, a non-destructive test methodology (NDT), is widely used for pavement evaluation/forensic analysis including, pavement thickness evaluation, bridge deck evaluation, locating voids under pavements, locating rebar and ducts. The GPR methodology developed for this study utilizes changes in the direct wave to locate fluid in the pavement joint. Direct wave GPR methods have been used in concrete structures (Sbartaï, Laurens, Rhazi, Balayssac, & Arliguie, 2007), soil water content measurement (Galagedara, Parkin, & Redman, 2003), and archaeological studies (Ernenwein, 2006; Weissling, 2012).

6.2 Experimental Program

Ten 10″ thick, 3′ square Portland cement based concrete slabs were constructed on an open graded aggregate base (1.5″ thick) (Figure 6.2). The concrete consisted of a typical INDOT paving mixture with a w/c of 0.42 and an air content of 6.2% (ASTM C231). Two 3/4″ dowel bars were placed in the forms on modified dowel baskets prior to casting the concrete (the baskets were modified to fit in the forms). The dowel bars were 7″ from the concrete surface which would be similar to the depth on a typical INDOT concrete pavement (though it should be noted they are not located at mid-depth in this study). After the concrete cured, saw-cut joints were placed by a professional saw-cutting service using field equipment using procedures that are typical for pavements in Indiana. The saw cuts were placed into the pavement perpendicular to the dowel bars using INDOT specifications to a depth of D/3 (3.3″). The first joint cut was 0.125″ wide cut to the D/3 (3.3″) depth. A second cut was then made at twice the width (0.25″) to a depth of 1.25″ (see Figure 6.2). After casting, the saw-cutting debris was removed and the slabs were covered with wet burlap and plastic for 48 hours to promote curing without the loss of moisture. After this period the joints were cut, and then the slabs were placed into an environmental chamber at 23+/-2°C (73.4°F) and 50+/-4% relative humidity to dry for 30 days. This drying period is meant to open space in the pores.

The ends of the joints were covered with an asphaltic tape and a border of silicone-rubber sealant. This creates a dam on either end of each slab, leaving a full depth joint through the entire length of the slab that can be filled with fluid from the surface. The experiments were conducted by first collecting GPR data on slabs with no fluid in joints, then various levels of fluid was added to the joint and GPR data collected. For the first set of experimental data was collected with the joint empty, with 2″ of fluid in the joint, with 3″ of fluid in the joint, and with the joint full of fluid. For the second set of slabs experiment data was collected with the joint empty, with 0.5, 1, 2, 3, and 4″ of fluid in the joint. The fluids consisted of water, 14% NaCl concentration by mass (1/2 brine) and 28% NaCl concentration by mass (brine).

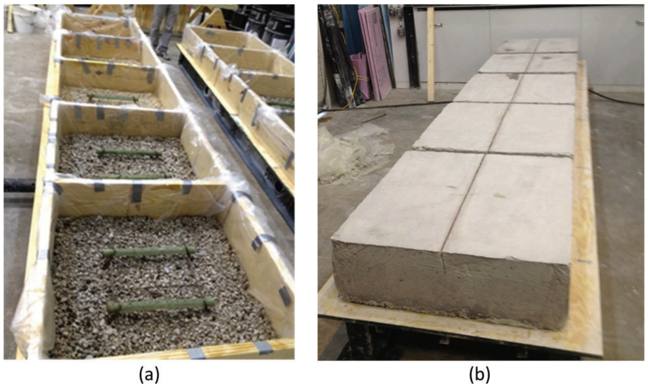
(a) (b)

Figure 6.2 (a) Concrete slab molds lined with plastic, 1.5″ open graded subbase and dowel bars on chairs and (b) slabs with molds removed after curing and cleaning.

6.3 Ground Penetrating Radar Background

Ground penetrating radar (GPR) has been utilized in many civil engineering applications over the last few decades. While lower frequency GPR (<900 MHz) has been used to find subsurface objects such as pipes and cables (Allred & Redman, 2010), higher frequency (1.5 GHz and 2.0 GHz) antennas are capable of detecting subsurface defects, such as delamination in bridge decks (Barnes & Trottier, 2004).

GPR is performed by transmitting polarized radio wave into an object (i.e., the concrete or joint) at a known center band frequency and measuring the amplitude and phase of the returned signal. Antennas with varying center band frequencies are frequently used and in general higher frequency antennas have finer resolution but often have a lower depth of penetration. Separate transmitting and receiving antennas are used in this study (i.e., bi-static setups). The manner in which the GPR antennas are coupled to the object they measure (i.e., air or ground coupled) is also important and in this study ground coupled antennas were used. The antennas are attached to a distance measuring instrument (DMI) (a small cart where one wheel that accurately records distance) while data is collected. Finally the polarization of the radar wave with respect to the joint is dependent on the orientation of the transmitting and receiving antennas with respect to the direction of motion as the system crosses the joint (seeFigure 6.3).

A total of more than 1,000 lines of GPR scanning data were collected in this study. The scan grid that consisted of lines spaced at 6″ (15.24 cm) in both directions along the slab (Figure 6.3a). The data was collected using two antenna orientations XX and YY (see Figure 6.3b), using 2.6 GHz, 1.6 GHz, 900 MHz and 400 MHz frequency antennas. Data was collected by scanning parallel to the joint and perpendicular to the joint.

It is also important to understand the data provided by a GPR measurement. GPR uses principles of scattering electromagnetic waves to locate objects that may be below a surface. The transmitting antenna transmits a radiating wave which will travel through an object (e.g., concrete, air in joint, fluid in joint) at a speed that is related to the electrical permittivity of the material). A portion of the wave can be reflected/scattered from the boundary (interface) or change in wave speed between materials. This scattering can be detected in the wave that is recorded by the receiving antenna. If the transmitter and receiver are kept at one location a time dependent history of the collection of waves that travel between the transmitter and receiver can be collected and this is known as a trace. The trace describes the amplitude of the received wave as a function of time (in nanoseconds) which corresponds to the depth from the surface. Many traces can be recorded as the antennas move along during the survey and can be stacked together in something known as a wiggle trace.

Figure 6.4 provides an illustration of a wiggle trace with every sixth trace shown. It can be noticed

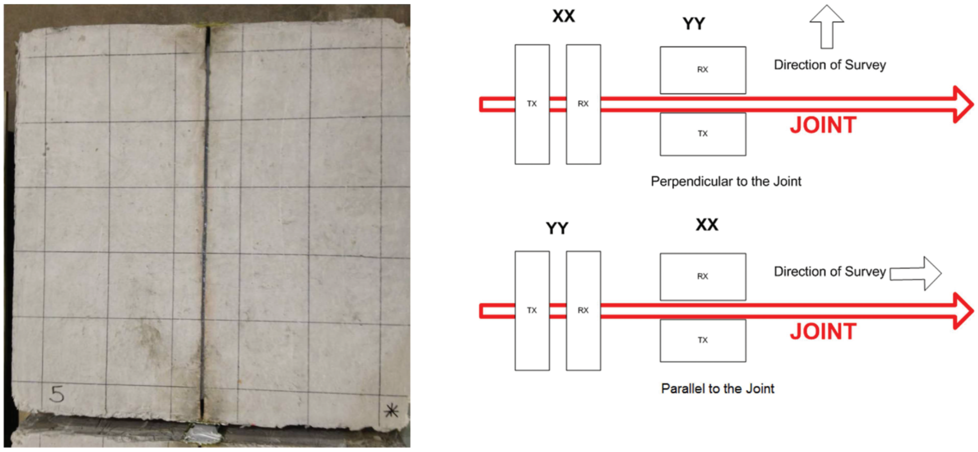

(a) (b)

Figure 6.3 (a) The grid used for scanning joints and (b) an illustration of the antenna orientation.

that the first and last traces of the 400 MHz wiggle trace and the first and last traces of the 900 MHz wiggle trace shown are very similar respectively and are taken when the antennas are directly over concrete. The traces in the center of the 400 MHz sample (show in red) however show a varying response in terms of the amplitude and timing of the wave between (2 and 8 ns) which corresponds to measurements that include the effect of the fluid in the saw-cut joint. The direct wave of the 900 MHz antenna over the joint (shown in red) is also greatly changed corresponding to the joint.

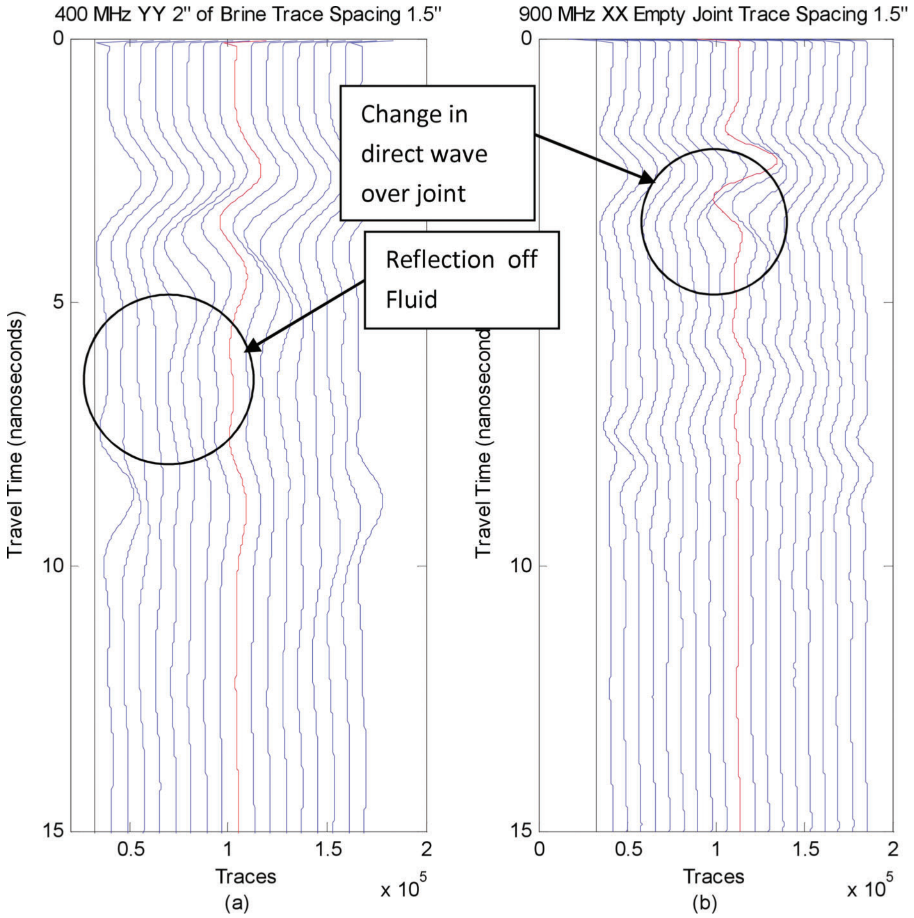

Figure 6.4 An illustration of a wiggle trace perpendicular to joint: (a) 400 MHz in the YY orientation, (b) 900 MHz in the XX orientation.

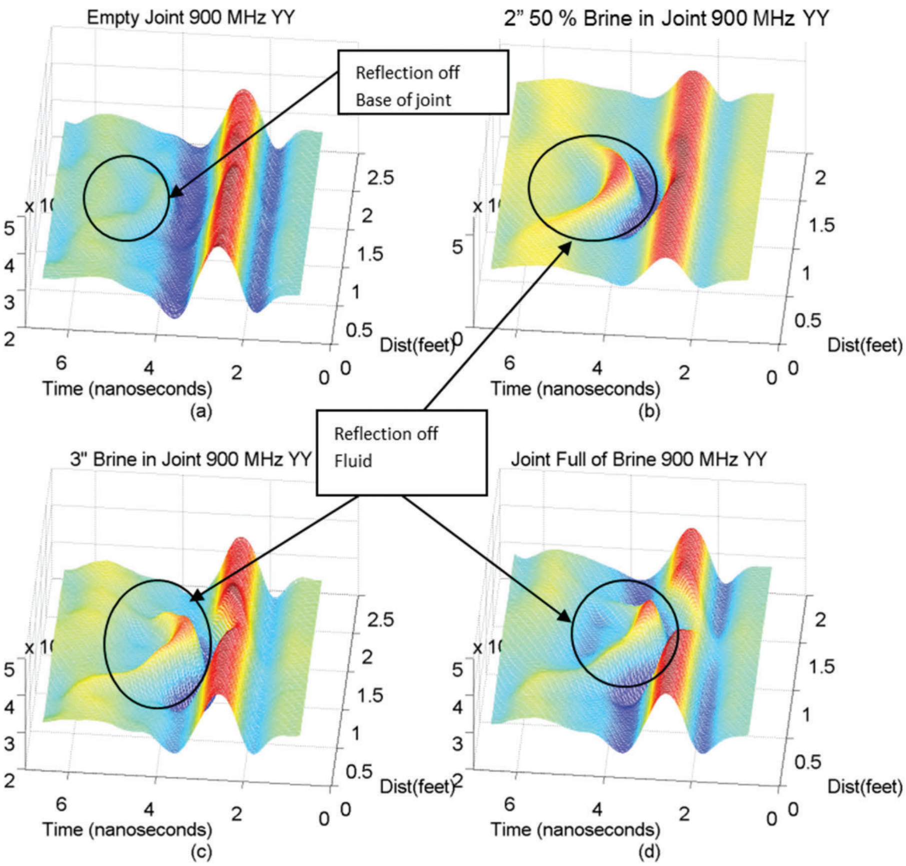

Figure 6.5 900 MHz antenna in the YY direction with the scan perpendicular to joint: (a) empty joint, (b) 2″ of 50% brine in the joint, (c) 3″ of brine in the joint, and (d) 4″ of brine in the joint (the z axis is amplitude). The dominating red reflection at approximately 3 nanoseconds is the coupling between the antenna and the concrete surface.

6.4 Ground Penetrating Radar: Fluid, Joint, and Dowel Depth

Figure 6.5 shows results from the ground penetrating radar with the scan perpendicular to joint, and four different levels of standing salt water (brine) in the saw-cut joint. The scan occurs across the entire width of the sample (2.5′) with a scan performed every 1/4″. While the x-axis illustrates the timing of the wave (similar to distance from the surface) the amplitude of the wave is show in the z-direction with the highest colors showing the highest amplitude (most red color). It can be seen that the GPR wave reflects off both the base of the saw cut (interface between air and concrete) and the fluid (interface of water or brine) in the saw cut. This reflection was visible for both the 1.6 GHz data and the 900 MHz data; however, the reflection from the fluid surface was more pronounced when the 900 MHz antenna was used. The reflection from the fluid has a higher amplitude and occurs at an earlier time (i.e., it is closer to the surface) than the reflection off the bottom of the joint.

At this point it is important to note that in addition to the reflections from the base of the joint or fluid it is possible to obtain a reflection from the dowel bars or baskets. INDOT has collected more than 1,000 miles of GPR with the antennas in the YY orientation and the dowels are a prominent feature in the data collected. This may be due to the dowels being placed further from the surface in the laboratory.

6.5 Ground Penetrating Radar Results: Waveform and Scalar Measures in the XX Orientation Perpendicular to Joint

Examination of the GPR direct waves showed changes differences between the responses collected over concrete, over the empty joint, and over the joint containing various levels for fluids (Figure 6.4). The shape of the direct wave of a trace collected over the empty joint (red trace) differs from the trace collected over concrete (blue trace) (Figure 6.6). Specifically, the trace over the empty joint shows a significant increase in wave amplitude, a decrease in travel time, and a more pronounced more peaked than that over the bulk concrete. As the level of the fluid increase past a certain point the shape of the direct wave of the traces collected over the joint increasingly becomes more like that of a trace collected on concrete. For the 1.6 GHz, and 900 MHz antennas more water is required for this change to be detectable and approximately 3″ of fluid is needed (see Figure 6.6).

In examining the data from Figure 6.6 it is clear that if the entire wave form needs to be reviewed for each measurement the use of the GPR technique may

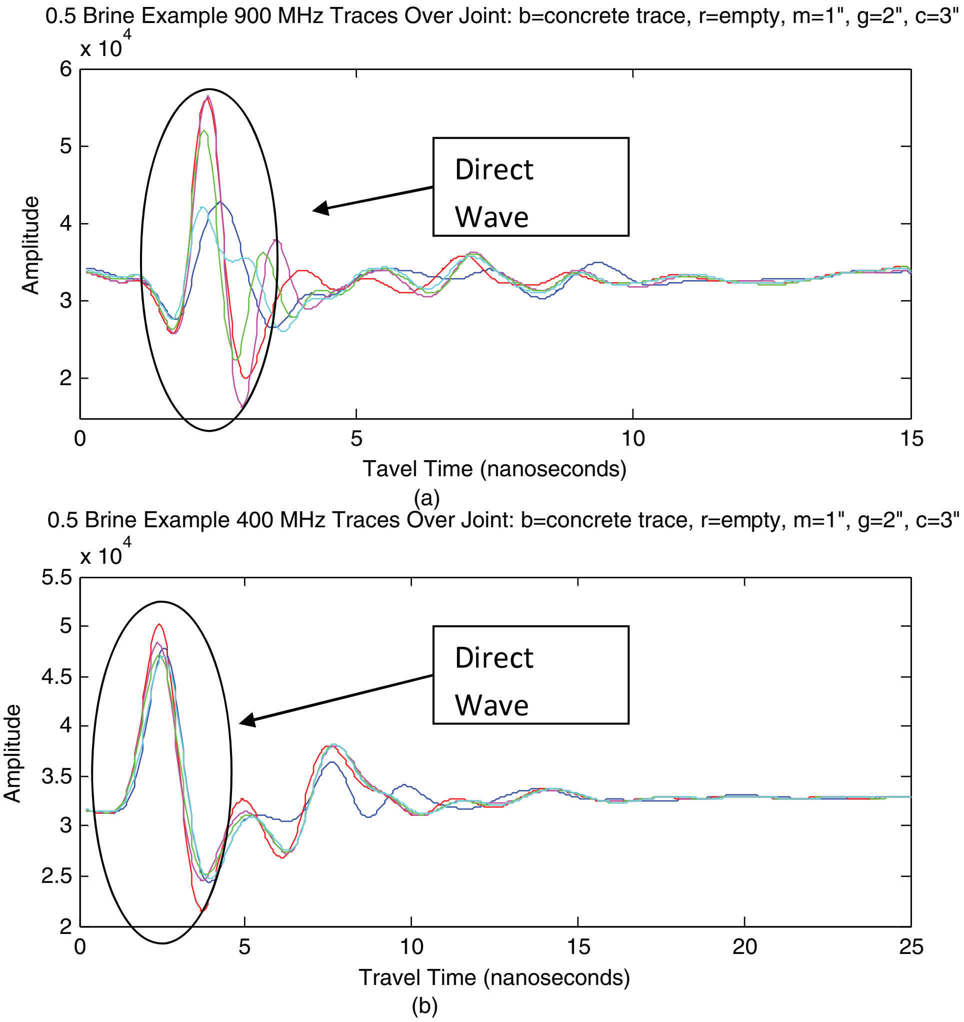

Figure 6.6 900 MHz antenna in the XX orientation: GPR traces: blue = concrete; red = empty joint, magenta = 1″ of 50% brine, green = 2″ of 50% brine, cayenne = 3″ of 50% brine.

become too complex to implement in the field. To simplify the interpretation of the waveforms the research team began to look at characteristic shapes of the direct wave to locate fluid in the joint. The initial possibilities for interpreting the waveform investigated use of the

1. maximum amplitude (Y value of the red points in Figure 6.7a),
2. travel time (X value of the red points in Figure 6.7a),
3. minimum amplitude (Y value of the cayenne point on left in Figure 6.7a),
4. pulse width (difference in X coordinates of cayenne point and the green point in Figure 6.7a),
5. maximum derivative (slope of lines with positive slope, Figure 6.7b),
6. minimum derivative (slope of lines with negative slope, Figure 6.7b), and
7. amplitude of the intersection of a derivative line (Y-value of the points marked with X on Figure 6.7b).

After an initial evaluation of these scalar values the travel time and pulse width were abandoned, the maximums and minimum amplitudes were plotted along with the maximum and minimum derivatives.

Examination of the maximum/minimum amplitude and the maximum/minimum derivative results showed similar trends (Figure 6.8). The amplitude and derivative data obtained using the 400 MHz antennas show proportional changes with the increase in fluid depth. The amplitude and derivative data was not proportional to the fluid depth for the data collected with the 900 MHz antenna presumably since there was some minimum depth of water that was needed before the direct wave would interact with the fluid and/or the change in air gap caused by the presence of the fluid. As a result it appears that the data collected using the 400 MHz antenna has the best for success in locating and easily quantifying the fluid in the joints.

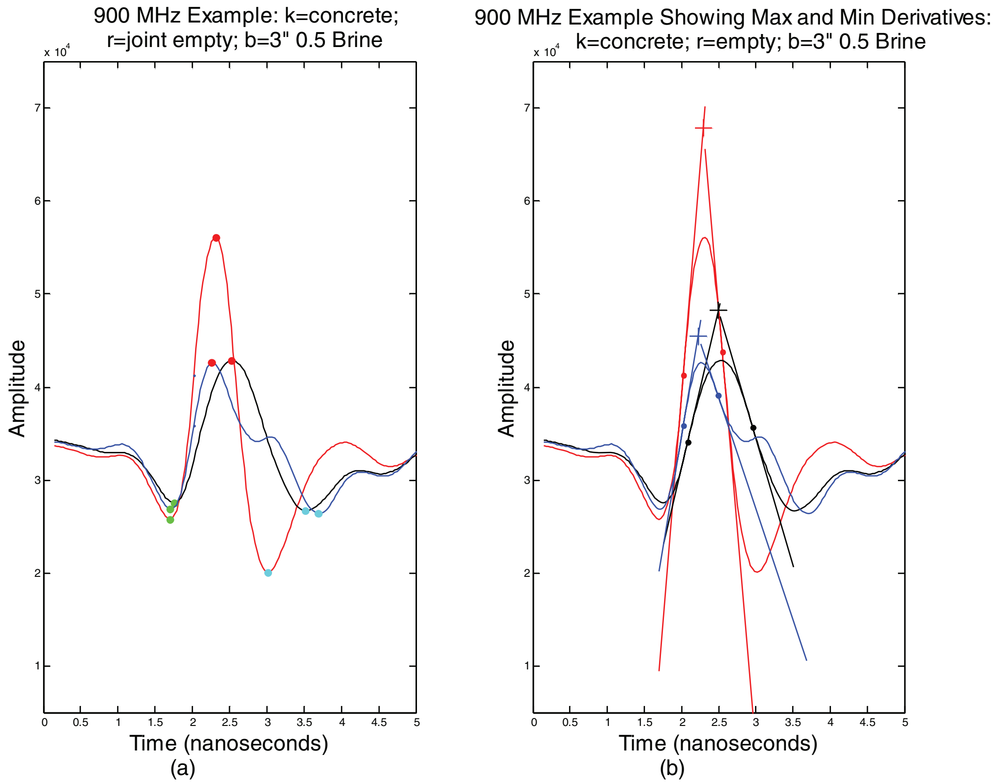

(a) (b)

Figure 6.7 Direct wave examples showing initial group of scalars selected.

6.6 Ground Penetrating Radar: Complexity-Invariant Distance Calculations

The complexity-invariance distance (CID) (Batista, Wang, & Keogh, 2011) methodology was used to quantify differences between the direct wave over concrete and over the joint. The CID provides a single number that can determine how similar the two waveforms are for classification purposes (Batista, Keogh, Tataw, & de Souza, 2014). Equation 6.1 can be used to compute the CID:

$$ID=\sqrt{\sum_{i=1}^{n}(q_i-c_i)^2}$$

$$\times\frac{max\left(\sqrt{\sum_{i=1}^{n}(q_i-q_{i+1})^2},\sqrt{\sum_{i=1}^{n}(c_i-c_{i+1})^2}\right)}{min\left(\sqrt{\sum_{i=1}^{n}(q_i-q_{i+1})^2},\sqrt{\sum_{i=1}^{n}(c_i-c_{i+1})^2}\right)} \qquad (6.1)$$

where qi is sample i of the trace over the concrete and ci is sample i over the trace of the joint.

The complete direct wave was not used for the CID calculations to avoid the influence of dowels/chairs that occur at the later time portions of the wave (i.e., greater depth). The influence of the dowel bars can be seen between 6 and 9 nanoseconds on the direct wave trace in Figure 6.9. The CID calculations were evaluated using two different segments of the direct wave (a short segment which comprised the measurements between 0 nanoseconds and the first peak amplitude and a long segment which comprised measurements between 0 nanoseconds and the time that the amplitude returns to an amplitude of 0). Ultimate the short segment was selected as it was the most consistent and least influenced by the dowel bars.

Figure 6.9 illustrates the direct trace measured using the 400 MHz antennas in the XX configuration taken perpendicular to joint with different layers of brine in the joint. The black trace was collected over the concrete surface (i.e., away from the saw cut) while the red trace was collected directly over the joint. Again the later portion of the curve (times greater than 6 ns) reflects the influence of the dowel/chair.

For the 400 MHz data, the CID magnitude of both the short segment and long segment decreased proportionally with an increase in fluid in the joint (see Figure 6.9 and Figure 6.10) and little difference is observed for the joints that are fuller. The 900 MHz and 1.6 GHz data did not decrease proportionally, and therefore did not provide as much information on the presence of fluid in the joint.

The CID has the advantage that it is simpler to interpret rather than using a complex waveform. To provide context: two perfectly similar traces would have a CID of 0. However in practice there is always some variation between the waves so 0 is not measured. As a result, when the CID falls below a certain threshold value, the potential is high that fluid has gathered in the joint behind the joint sealant. Based on data shown it is fair to assume that when the CID falls to less than ½ the value of the surrounding joints there is a strong possibility of fluid in the joint. The CID of the short segment of the direct wave from the trace and derivatives can be calculated and used to locate the joints with the high probability of fluid.

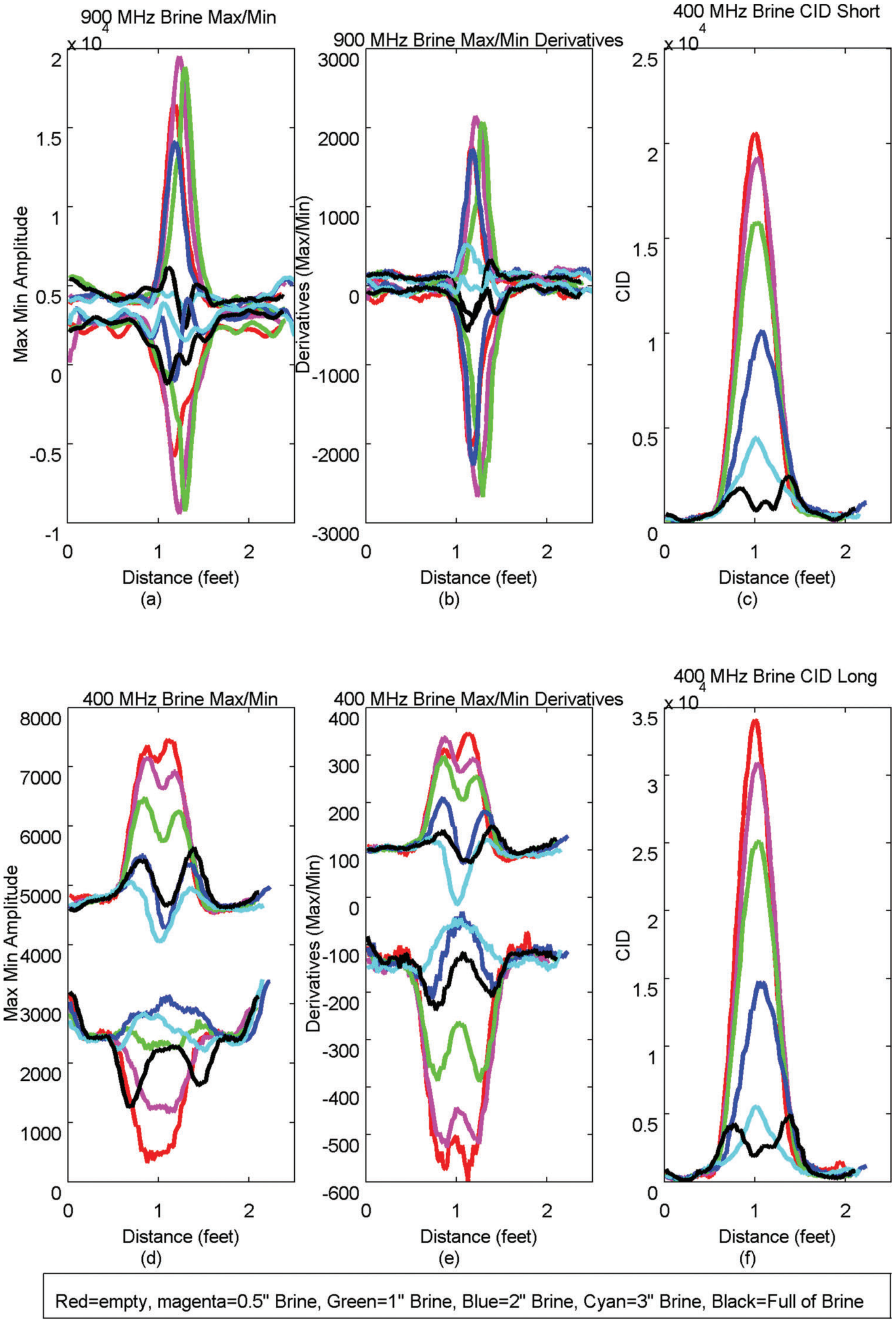

Figure 6.8 (a) 900 MHz antenna in the XX orientation—GPR direct wave maximums and minimum amplitudes, (b) 900 MHz antenna in the XX orientation—GPR direct wave maximum and minimum derivatives, (c) 400 MHz antenna in the XX orientation—CID calculated using the short wave segment (d) 400 MHz antenna in the XX orientation—GPR maximums and minimum amplitudes (e) 400 MHz antennal in the XX orientation—GPR maximum and minimum derivatives, (f) 400 MHz antenna in the XX orientation—CID calculated using the long wave segment.

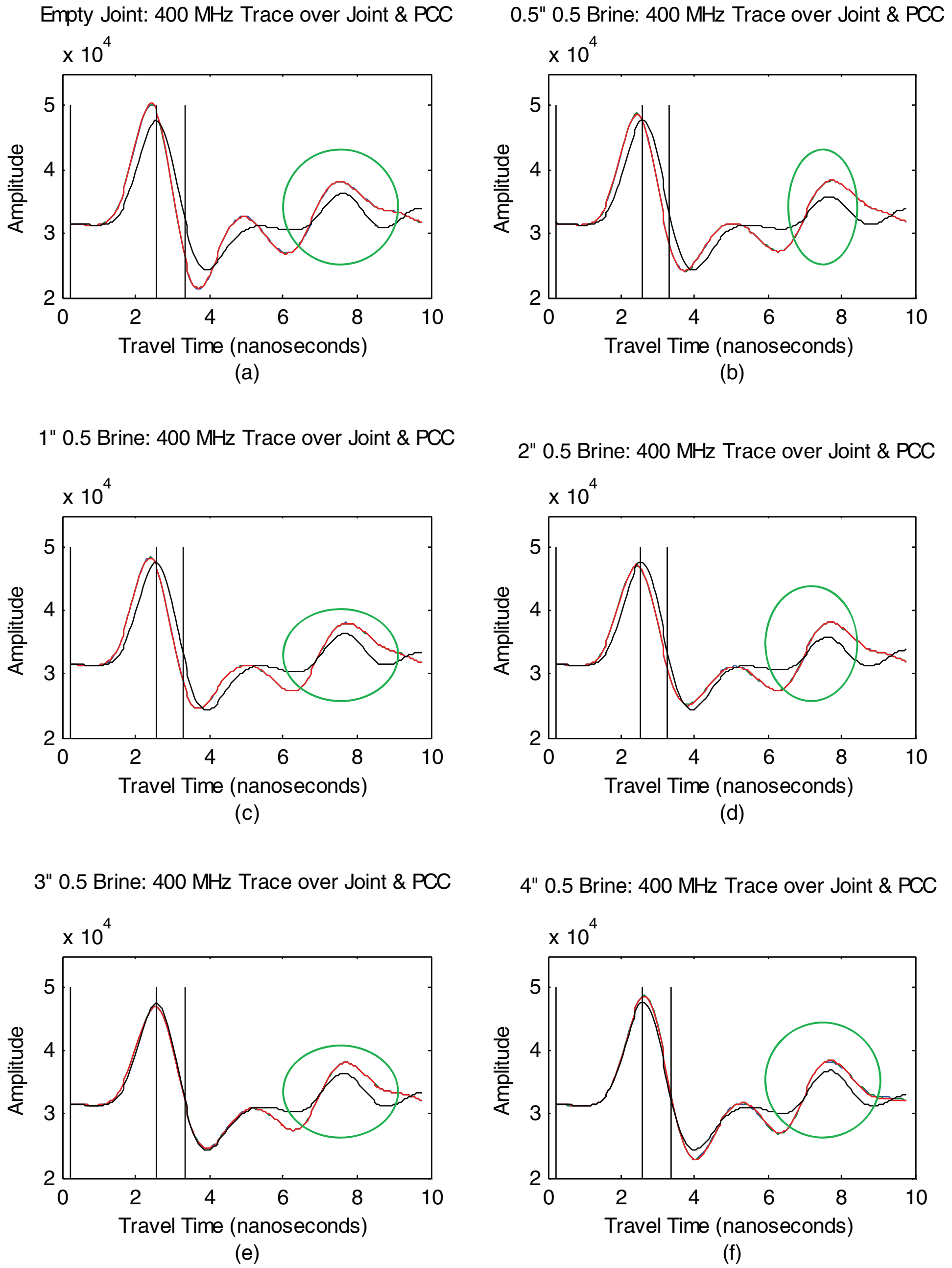

Figure 6.9 GPR collected on brine treated pad; black trace is collected on concrete, red trace collected over joint, the green ellipse shows the reflection that is due to the dowel/chair: (a) 0″, (b) 0.5″, (c) 1″, (d) 2″, (e) 3″, (f) 4″ of 50% brine.

6.7 Conclusions

Midwestern states have observed premature joint deterioration in jointed plain concrete pavements. It has been proposed that this deterioration occurs when the joint sealants fail allowing fluid to collect in the saw-cut joint. This can result in hydraulic pressure, osmotic pressure, or deleterious phases that damage the concrete. To effectively apply low cost corrective actions early detection of fluid in the joints is needed. Ground penetrating radar (GPR) was used effectively to detect fluid accumulation in the saw-cut joint behind the joint sealant in both the XX and YY antenna configurations. The typical GPR waveforms are difficult and time consuming to interpret. A signal processing approach, referred to as the CID, was used to obtain a single number that reflects the potential for fluid in the joint. It is proposed that the computed CID can be used with the minimum of the derivative of the wave form to estimate which joints may contain fluid and which joint sealant sections may need to be repaired or when a larger joint maintenance effort be performed to seal the joints or the concrete.

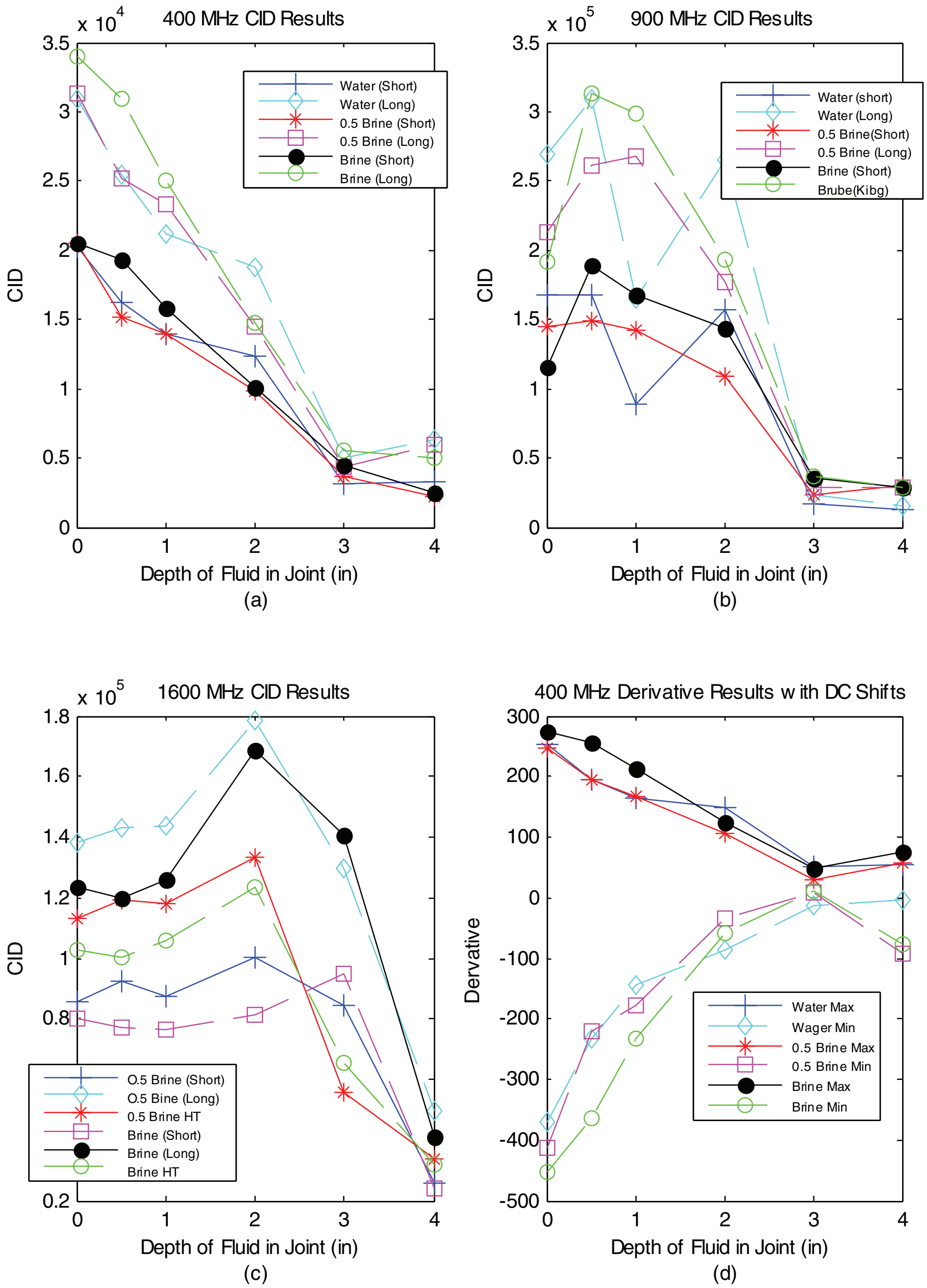

Figure 6.10 CID results for the 400 MHz antenna in the XX direction for differing depths of brine in the joint.

7. SUMMARY AND CONCLUSIONS

Midwestern states have observed premature joint deterioration in jointed plain concrete pavements. It has been proposed that this deterioration occurs when the joint sealants fail allowing fluid to collect in the saw-cut joint. Problems of joint deterioration (caused by water ingress, freezing and or salt reaction) have emerged which can shorten the life of the pavement requiring expensive and invasive repairs. To effectively apply low cost corrective actions early detection of fluid in the joints is needed. Concrete pavements can be expected to provide a relatively long service life. This project investigated the use of electrical resistivity and ground penetrating radar as two techniques to detect water trapped in a pavement joint.

7.1 Electrical Measurements at the Joint

Electrical measurements on laboratory slab specimens with standard joints were conducted using a Schlumberger array of varying spacing. The degree of saturation of the concrete surrounding the joint and the level of sitting fluid in the joint was assessed using varying probe spacings and orientations with respect to the axis of the joint.

Data suggests that electrical measurements conducted on concrete joints that have a high degree of saturation, of which thermal cycling will likely promote joint deterioration, are independent of probe spacing and orientation. This appears to be a method that shows promise to assess the degree of saturation of concrete surrounding the joint.

Furthermore, the presence of fluid sitting in a joint, surrounded by concrete with a lower degree of saturation, could be accomplished by rotation of narrowly spaced electrode array. Specifically, joints that do not have standing water show a decrease in resistivity as the probe is oriented more perpendicular to the joint, which decreased the effective width of the joint. The presence of solution in the joint manifests itself in the opposite fashion, in which the resistivity will decrease as the probe is oriented more along the axis of the joint. This appears to be an effective method to assess joint drainage. If joint drainage is poor, the concrete surrounding the joint will more quickly reach a critical degree of saturation where thermal cycling will lead to premature deterioration.

It is worth mentioning that specific values of resistivity are dependent on a large number of factors that are independent to each pavement and environment, including solution in the pores, degree of saturation, and temperature (Spragg, Bu, et al., 2013; Spragg, Villani, et al., 2013). As such, specific ranges of resistivity values that will lead to premature deterioration are difficult to establish. Instead, the trends discussed above should be assessed. Another potential calibration is normalizing by measurements conducted using widely spaced probes away from a jointed area in an area with well-performing concrete.

7.2 Electrical Measurements with Varying Temperature

The electrical response was measured for mortars subjected to a temperature cycle from 23°C to -35°C, with varying degrees of saturation, and varying salt concentrations. The resistivity increased as the degree of saturation was reduced due to the reduction in the volume of the conductive medium and increase in tortuosity. The resistivity decreased as the concentration of NaCl increased due to the increased ionic concentration which facilitates electrical conduction. The resistivity gradually increased as temperature was decreased until the phase transformation temperature (i.e., ice formation), after which time the resistance increased more rapidly. The increase in resistivity can be described using an Arrhenius law for conduction from 23°C due to the phase transformation temperature; however, at temperatures lower than the phase transition temperature, the responses is more complex due to a reduction in conducting fluid and a change in solution concentration. The influence of the degree of saturation and salt concentration on the amount of activation energy seemed relatively small. Changes in resistivity were detected when cracking occurred in the sample. The magnitude of these changes was similar to that detected using changes in the ultrasonic wave speed.

7.3 Ground Penetrating Radar Measurements at the Joint

Ground penetrating radar (GPR) was used effectively to detect fluid accumulation in the saw-cut joint behind the joint sealant. The typical GPR waveforms are difficult and time consuming to interpret. Features of the wave form (amplitude and derivative) indicate the presence of fluid; however, the XX antenna configuration with the 400 MHz antennas was the most promising due to proportionality with the fluid present in the joint. A signal processing approach termed the complexity-invariance distance (CID) approach, was used to obtain a single number that reflects the potential for fluid in the joint. Scalar waveform features and the computed CID can be used to estimate which joints may contain fluid thereby providing insights into which joint sealant sections may need to be repaired or when a sufficient number of joints may contain fluid suggesting a larger joint maintenance effort be performed to seal the joints or the concrete.

8. RECOMMENDATIONS

Concrete pavements can be expected to provide a relatively long service life. However in some cases, problems of joint deterioration (caused by water ingress, freezing and or salt reaction) have emerged which can shorten the life of the pavement requiring expensive and invasive repairs. This project investigated the use of electrical resistivity and ground penetrating radar as two techniques to detect premature joint deterioration.

8.1 Early Detection Systems

It has been shown that areas that are exposed to water and salts have different electrical properties than areas which are not exposed to these conditions. Ground penetrating radar can be used to gain a general understanding of the fluid level in the joint without requiring the removal of backer rod and silicone sealant. Currently, this process would only provide a binary solution to say whether or not fluid exists in the joint beyond a certain depth. However, refinement of the process and a statistical analysis of the differences between maximum amplitudes of regular and cross polarized scans on a variety of pavements could provide the ability to determine the depth of fluid in a joint.

Direct measurement of electrical resistivity of the concrete from the surface can also be used to determine if fluid exist in the joint beyond a threshold decided to be indicative of susceptibility to joint deterioration. Like the GPR process, this method will be influenced by many factors independent to each specific pavement. With further investigation and the compilation of a statistical data set, it may be possible to determine a relationship between resistivity attenuation, measured at a set angle with a set array of electrodes, and the depth of fluid within the joint. In both of these processes results should be compared to results on a section of known condition, preferable an area with an empty joint.

8.2 Mitigating Susceptibility to Deterioration

It had been shown previously that SME-PS is a beneficial concrete sealant in laboratory settings, and can significantly reduce damage that is instigated by freezing and thawing cycles. It is thought that this sealant provides a solution to remediate pavements that have been deemed susceptible to damage in order to mitigate this potential. SME-PS also seems to provide an opportunity to effectively seal newly constructed pavement joints and prevent fluid ingress before susceptibility to damage can become an issue.

Field applications have begun to demonstrate this practice on both remedial and new construction projects. These trials have shown SME-PS application to be a fairly simple process as long as a few key points, such as temperature and DOS, are managed. Qualitative data taken to-date has not shown any divergence from the expected performance of this sealant. However, long term analysis is needed in order to quantify the effect of SME-PS on the ingress of fluids in these joints and its ability to mitigate susceptibility to deterioration.

9. ACKNOWLEDGMENTS AND DISCLAIMER

The research described in this report was conducted as part of SPR-3623. The contents of this report reflect the views of the authors, who are responsible for the facts and the accuracy of the data presented herein. The contents do not necessarily reflect the official views or policies of the Indiana Department of Transportation or the Federal Highway Administration at the time of publication. This report does not constitute a standard, specification, or regulation. Certain commercial products are identified in this report to specify the materials used and procedures employed. In no case does such identification imply endorsement or recommendation by Purdue University, nor does it indicate that the products are necessarily the best available for the purpose. The experiments described in this study were conducted at the Pankow Materials Laboratory at Purdue University, and the authors are grateful for the support which has made its operation possible.

REFERENCES

Allred, B. J., & Redman, J. D. (2010). Location of agricultural drainage pipes and assessment of agricultural drainage pipe conditions using ground penetrating radar. *J Environ Eng Geophys*, *15*, 119–134. http://dx.doi.org/10.2113/JEEG15.3.119

ASTM. (2009a). *ASTM C597: Standard test method for pulse velocity through concrete*. http://dx.doi.org/10.1520/C0597-09

ASTM. (2009b). *ASTM E1225: Standard test method for thermal conductivity of solids by means of the guarded-comparative-longitudinal heat flow technique*.

ASTM. (2012a). *ASTM C1202: Standard test method for electrical indication of concrete's ability to resist chloride ion penetration*. http://dx.doi.org/10.1520/C1202-12

ASTM. (2012b). *ASTM C305: Standard practice for mechanical mixing of hydraulic cement pastes and mortars of plastic consistency*. http://dx.doi.org/10.1520/C0305-12

ASTM. (2012c). *ASTM D5470: Standard test method for thermal transmission properties of thermally conductive electrical insulation materials*. http://dx.doi.org/10.1520/D5470-12

Barnes, C. L., & Trottier, J.-F. (2004). Effectiveness of ground penetrating radar in predicting deck repair quantities. *J Infrastruct Syst*, *10*, 69–76. http://dx.doi.org/10.1061/(ASCE)1076-0342(2004)10:2(69)

Batista, G., Wang, X., & Keogh, E. (2011). A complexity-invariant distance measure for time series. In *Eleventh SIAM International Conference on Data Mining (SDM 2011)* (pp. 699–710).

Batista, G. E. A.P. A., Keogh, E. J., Tataw, O. M., & de Souza, V. M. A. (2014). CID: An efficient complexity-invariant distance for time series. *Data Min Knowl Discov*, *28*(3), 634–669. http://dx.doi.org/10.1007/s10618-013-0312-3

Cao, J., & Chung, D. D. L. (2002). Damage evolution during freeze–thaw cycling of cement mortar, studied by electrical resistivity measurement. *Cem Concr Res*, *32*(10), 1657–1661. http://dx.doi.org/10.1016/S0008-8846(02)00856-6

Cao, J., Wen, S., & Chung, D. D. L. (2001). Defect dynamics and damage of cement-based materials, studied by electrical resistance measurement. *J Mater Sci*, *36*(18), 4351–4360. http://dx.doi.org/10.1023/A:1017901929264

Castro, J., Spragg, R., & Weiss, J. (2012). Water absorption and electrical conductivity for internally cured mortars with a W/C between 0.30 and 0.45. *J Mater Civ Eng*, *24*(2), 223–231. http://dx.doi.org/10.1061/(ASCE)MT.1943-5533.0000377

Chung, D. D. L. (2003). Damage in cement-based materials, studied by electrical resistance measurement. *Mater Sci Eng R Reports*, 42, 1–40. http://dx.doi.org/10.1016/S0927-796X(03)00037-8

Coates, K. C., Mohtar, S., Tao, B., & Weiss, J. (2009). Can soy methyl esters reduce fluid transport and improve durability of concrete? *Transp Res Rec J Transp Res Board*, *2113*, 22–30. http://dx.doi.org/10.3141/2113-03

Curran, P. N., & McCarter, W. J. (1984). The electrical response characteristics of setting cement paste. *Mag Concr Res*, *36*(126), 42–49. http://dx.doi.org/10.1680/macr.1984.36.126.42

Debenedetti, P. G., & Stanley, H. E. (2003). Supercooled and glassy water. *Phys Today*, *56*, 40–46. http://dx.doi.org/10.1063/1.1595053

Dullien, F. (1992). *Porous media: Fluid transport and pore structure,* 2nd ed (p. 574). San Diego: Academic Press.

Ernenwein, E. G. (2006). Imaging in the ground-penetrating radar near-field zone: A case study from New Mexico, USA. *Archaeol Prospect*, *13*(2), 154–156. http://dx.doi.org/10.1002/arp.286

Fagerlund, G. (1975). The significance of critical degrees of saturation at freezing of porous and brittle materials. In *Durability of Concrete: ACI SP 47-2* (pp. 13–66). Detroit, MI: American Concrete Institute.

Farnam, Y., Bentz, D., Hampton, A., & Weiss, J. (2014). Acoustic emission and low temperature calorimetry study of freeze and thaw behavior in cementitious materials exposed to sodium chloride salt. *Transp Res Board Rec*, *2441*, 81–90.

Farnam, Y., Bentz, D., Sakulich, A., Flynn, D., & Weiss, J. (2014). Measuring freeze and thaw damage in mortars containing deicing salt using a low-temperature longitudinal guarded comparative calorimeter and acoustic emission. *Adv Civ Eng Mater*, *3*(1), 315–337. http://dx.doi.org/10.1520/ACEM20130095

Farnam, Y., Dick, S., Wiese, A., Davis, J., Bentz, D., & Weiss, J. (2014). *The influence of calcium chloride deicing salt on phase changes and damage development in cementitious materials.* Manuscript submitted for publication to Cement and Concrete Composites.

Farnam, Y., Geiker, M. M. R., Bentz, D., & Weiss, J. (2014). *Using acoustic emission waveform characterization to ascertain where cracks originate in concrete*. Manuscript submitted for publication to Cement and Concrete Composites.

Farnam, Y., & Todak, H., Spragg, R., & Weiss, J. (2015). Electrical response of mortar with different degrees of saturation and deicing salt solutions during freezing and thawing. *Cement and Concrete Composites*, *59*, 49–59. http://dx.doi.org/10.1016/j.cemconcomp.2015.03.003

Farnam, Y., Wiese, A., Bentz, D., Davis, J., & Weiss, J. (2015). Damage development in cementitious materials exposed to magnesium chloride deicing salt. *Construction and Building Materials*, *93*, 384–392. http://dx.doi.org/10.1016/j.conbuildmat.2015.06.004

Galagedara, L. W., Parkin, G. W., & Redman, J. D. (2003). An analysis of the ground-penetrating radar direct ground wave method for soil water content measurement. *Hydrol Process*, *17*(18), 3615–3628. http://dx.doi.org/10.1002/hyp.1351

Golias, M., Castro, J., Peled, A., Nantung, T., Tao, B., & Weiss, W. J. (2012). Can soy methyl esters improve concrete pavement joint durability? *Transp Res Rec J Transp Res Board*, *2290*, 60–68. http://dx.doi.org/10.3141/2290-08

Indiana Department of Transportation. (2011). Concrete paving. In *Highway certified technician program training manual* (pp. 1–14). Indianapolis, IN: INDOT.

Jones, W., & Farnam, Y., Imbrock, P., Spiro, J., Villani, C., Olek, J., & Weiss, W. J. (2013). *An Overview of Joint Deterioration in Concrete Pavement: Mechanisms, Solution Properties, and Sealers*. West Lafayette, IN: Purdue University. http://dx.doi.org/10.5703/1288284315339

Julio-Betancourt, G. A., & Hooton, R. D. (2004). Study of the Joule effect on rapid chloride permeability values and evaluation of related electrical properties of concretes. *Cem Concr Res*, *34*(6), 1007–1015. http://dx.doi.org/10.1016/j.cemconres.2003.11.012

Keller, G. V. (1966). Dipole method for deep resistivity studles. *Geophysics*, *31*(6), 1088. http://dx.doi.org/10.1190/1.1439842

Li, W., Pour-Ghaz, M., Castro, J., & Weiss, J. (2012). Water absorption and critical degree of saturation relating to freeze-thaw damage in concrete pavement joints. *J Mater Civ Eng*, *24*(3), 299–307. http://dx.doi.org/10.1061/(ASCE)MT.1943-5533.0000383

Litvan, G. (1976). Frost action in cement in the presence of de-icers. *Cem Concr Res*, *6*(3), 351–356. http://dx.doi.org/10.1016/0008-8846(76)90097-1

Liu, Y., & Presuel-Moreno, F. (2014). Effect of elevated temperature curing on compressive strength and electrical resistivity of concrete with fly ash and GGBS. *Mater J*, *111*(5), 531–542. http://dx.doi.org/10.14359/51686913

McCarter, W. J., Forde, M. C., Whittington, H. W., & Ravindrarajan, S. (1982). Resistivity characteristics of concrete. *ICE Proc*, *73*(1), 223–224. http://dx.doi.org/10.1680/iicep.1982.1993

Morris, W., Moreno, E. I., & Sagüés, A. A. (1996). Practical evaluation of resistivity of concrete in test cylinders using a Wenner array probe. *Cem Concr Res*, *26*(12), 1779–1787. http://dx.doi.org/10.1016/S0008-8846(96)00175-5

Niemuth, M. (2004). *Using impedance spectroscopy to detect flaws in concrete* (Master's thesis). West Lafayette, IN: Purdue University.

Nokken, M., Boddy, A., Wu, X., & Hooton, R. (2008). Effects of temperature, chemical, and mineral admixtures on the electrical conductivity of concrete. *J ASTM Int*, *5*(5), 101296. http://dx.doi.org/10.1520/jai101296

Olson, R. A., Christensen, B. J., Coverdale, R. T., Ford, S. J. Moss, G M., Jennings, H. M., Garboczi, E. J. (1995). Interpretation of the impedance spectroscopy of cement paste via computer modelling: Part III—Microstructural analysis of frozen cement paste. *J Mater Sci*, *30*, 5078–5086. http://dx.doi.org/10.1007/BF00356052

Osterminski, K., Polder, R. B., & Schießl, P. (2012). Long term behaviour of the resistivity of concrete. *Heron*, *57*(3), 211–230.

Peled, A., Torrents, J. M., Mason, T. O., Shah, S. P., & Garboczi, E. J. (2001). Electrical impedance spectra to monitor damage during tensile loading of cement composites. *ACI Mater J*, *98*, 313–322. http://dx.doi.org/10.14359/10400

Pour-Ghaz, M. (2011). *Detecting damage in concrete using electrical methods and assessing moisture movement in cracked concrete* (Doctoral dissertation). West Lafayette, IN: Purdue University. Retrieved from http://docs.lib.purdue.edu/dissertations/AAI3481128/

Pour-Ghaz, M., Niemuth, M., & Weiss, J. (2013). Use of electrical impedance spectroscopy and conductive surface films to detect cracking and damage in cement based materials. International Concrete Abstracts Portal, Special Publications, *292*, 1–16. http://dx.doi.org/10.14359/51686285

Pour-Ghaz, M., Rajabipour, F., Couch, J., & Weiss, J. (2009). Numerical and experimental assessment of unsaturated fluid transport in saw-cut (notched) concrete elements. International Concrete Abstracts Portal (Document SP266-06), Special Publications, *266*, 73–85. http://dx.doi.org/10.14359/51663273

Qian, Y., Farnam, Y., & Weiss, J. (2014). Using acoustic emission to quantify freeze–thaw damage of mortar saturated with NaCl solutions. In J. Olek & J. Weiss (Eds.), *Proceedings of the 4th International Conference on the Durability of Concrete Structures* (pp. 32–37). West Lafayette, IN: Purdue University. http://dx.doi.org/10.5703/1288284315379

Rajabipour, F. (2006). *Insitu electrical sensing and material health monitoring in concrete structure* (Doctoral dissertation). West Lafayette, IN: Purdue University. Retrieved from http://docs.lib.purdue.edu/dissertations/AAI3259972/

Ramezanianpour, A. A., Pilvar, A., Mahdikhani, M., & Moodi, F. (2011). Practical evaluation of relationship between concrete resistivity, water penetration, rapid chloride penetration and compressive strength. *Constr Build Mater*, *25*(5), 2472–2479. http://dx.doi.org/10.1016/j.conbuildmat.2010.11.069

Raoufi, K., Radlinska, A., Nantung, T., & Weiss, J. (2009). Methodology for determining the timing of saw cutting in concrete pavements. *Transp Res Rec J Transp Res Board*, 2081, 110–117. http://dx.doi.org/10.3141/2081-12

Sant, G., Rajabipour, F., & Weiss, J. (2008). The influence of temperature on electrical conductivity measurements and maturity predictions in cementitious materials during hydration. *Indian Concr J*, *82*, 7–16.

Sato, T., & Beaudoin, J. J. (2003). An AC impedance spectroscopy study of freezing phenomena in wollastonite micro-fibre reinforced cement paste. In R. K. Dhir, M. D. Newlands, & K. A. Paine (Eds.), *Role of concrete in sustainable development* (pp. 379–388). London, UK: Thomas Telford, Ltd.

Sbartaï, Z. M. M., Laurens, S., Rhazi, J., Balayssac, J. P., & Arliguie, G. (2007). Using radar direct wave for concrete condition assessment: Correlation with electrical resistivity. *J Appl Geophys*, *62*(4), 361–374. http://dx.doi.org/10.1016/j.jappgeo.2007.02.003

Scherer, G. W. (1999). Crystallization in pores. *Cem Concr Res*, *29*(8), 1347–1358. http://dx.doi.org/10.1016/S0008-8846(99)00002-2

Shi, X., Fay, L., Peterson, M. M., Yang, Z. (2010). Freeze–thaw damage and chemical change of a Portland cement concrete in the presence of diluted deicers. *Mater Struct*, *43*(7), 933–946. http://dx.doi.org/10.1617/s11527-009-9557-0

Shimizu, Y. (1928). An electrical method for measuring the setting time of Portland cement. *Mill Sect Concr*, *32*(5), 111–113.

Snyder, K. A. (2001). The relationship between the formation factor and the diffusion coefficient of porous materials saturated with concentrated electrolytes?: theoretical and experimental considerations. *Concr Sci Eng*, *3*, 216–224.

Sohn, D., & Mason, T. O. (1998). Electrically induced microstructural changes in Portland cement pastes. *Adv Cem Based Mater*, *7*(3–4), 81–85. http://dx.doi.org/10.1016/S1065-7355(97)00056-4

Spragg, R. (2013). *The rapid assessment of transport properties of cementitious materials using electrical methods* (Master's thesis). West Lafayette, IN: Purdue University. Retrieved from http://docs.lib.purdue.edu/dissertations/AAI1549494/

Spragg, R., Bu, Y., Snyder, K., Bentz, D., & Weiss, J. (2013). *Electrical testing of cement-based materials: role of testing techniques, sample conditioning, and accelerated curing* (Joint Transportation Research Program Publication No. FHWA/IN/JTRP-2013/28). West Lafayette, IN: Purdue University. http://dx.doi.org/10.5703/1288284315230

Spragg, R., Villani, C., Snyder, K., Bentz, D., Bullard, J. W., & Weiss, J. (2013). Factors that influence electrical resistivity measurements in cementitious systems.*Transp Res Rec J Transp Res Board*, *2342*, 90–98. http://dx.doi.org/10.3141/2342-11

Spragg, R. P., Castro, J., Li W., Pour-Ghaz, M., Huang, P.-T., & Weiss, J. (2011). Wetting and drying of concrete using aqueous solutions containing deicing salts. *Cem Concr Compos*, *33*(5), 535–542. http://dx.doi.org/10.1016/j.cemconcomp.2011.02.009

Spragg, R. P., Castro, J., Nantung, T., Paredes, M., & Weiss, J. (2012). Variability analysis of the bulk resistivity measured using concrete cylinders (Paper ID ACEM104596). *Adv Civ Eng Mater*, *1*(1), 1–17. http://dx.doi.org/10.1520/ACEM104596

Sutter, L., Peterson, K., Julio-Betancourt, G., Hooton, D., Van Dam, T., & Smith, K. (2008). *The deleterious chemical effects of concentrated deicing solutions on Portland cement concrete* (Study SD2002-01, Final Report, prepared by Michigan Tech Transportation Institute). Pierre, SD: South Dakota Department of Transportation.

Sutter, L., Peterson, K., Touton, S., Van Dam, T., & Johnston, D. (2006). Petrographic evidence of calcium oxychloride formation in mortars exposed to magnesium chloride solution. *Cem Concr Res*, *36*(8), 1533–1541. http://dx.doi.org/10.1016/j.cemconres.2006.05.022

Taillet, E., Lataste, J. F., Rivard, P., & Denis, A. (2014). Non-destructive evaluation of cracks in massive concrete using normal dc resistivity logging. *NDT & E Int*, *63*, 11–20. http://dx.doi.org/10.1016/j.ndteint.2014.01.001

Tang, L., Nilsson, L.-O., & Basheer, P. A. M. (2011). *Resistance of concrete to chloride ingress: Testing and modelling*. Boca Raton, FL: CRC Press.

Taylor, P., Sutter, L., & Weiss, J. (2012). *Investigation of deterioration of joints in concrete pavements* (Final Report, FHWA Contract No. DTFH61-06-H-00011 Work Plan 26). Washington, DC: Federal Highway Administration.

Valenza, J. J., & Scherer, G. W. (2005). Mechanisms of salt scaling. *Mater Struct*, *38*(4), 479–488. http://dx.doi.org/10.1007/BF02482144

Van Beek, A., & Hilhorst, M. A. (1999). Dielectric measurements to characterize the microstructural changes of young concrete. *Heron*, *44*(1), 3–17.

Villagrán Zaccardi, Y. A., Fullea García, J., Huélamo, P., & Di Maio, Á. A. (2009). Influence of temperature and humidity on Portland cement mortar resistivity monitored with inner sensors. *Mater Corros*, *60*(4), 294–299. http://dx.doi.org/10.1002/maco.200805075

Villani, C., & Farnam, Y., Washington, T., Jain, J., & Weiss, W. J. (2015). *Performance of conventional Portland cement and calcium silicate based carbonated cementitious systems during freezing and thawing in the presence of calcium chloride deicing salts.* Manuscript submitted for publication to Transportation Research Board.

Wei, X., & Xiao, L. (2014). Kinetics parameters of cement hydration by electrical resistivity measurement and calorimetry. *Adv Cem Res*, *26*(4), 187–193. http://dx.doi.org/10.1680/adcr.13.00034

Weiss, J., Snyder, K., Bullard, J., & Bentz, D. (2012). Using a saturation function to interpret the electrical properties of partially saturated concrete. *J Mater Civ Eng*, *25*(8), 1097–1106. http://dx.doi.org/10.1061/(ASCE)MT.1943-5533.0000549

Weiss, W., Shane, J., Mieses, A., Mason, T. O., & Shah, S. P. (1999). Aspects of monitoring moisture changes using electrical impedance spectroscopy. In *Proceedings of the second international research seminar on self-desiccation and its importance in concrete technology* (pp. 31–48). Lund, Sweden: Lund Institute of Technology.

Weissling, B. P. (2012). Historical tracks and trail resources as delineated by near-field ground-penetrating radar: Two case studies. *Archaeol Prospect*, *19*(1), 1–6. http://dx.doi.org/10.1002/arp.424

Wen, S., & Chung, D. D. L. (2000). Damage monitoring of cement paste by electrical resistance measurement. *Cem Concr Res*, *30*(12), 1979–1982. http://dx.doi.org/10.1016/S0008-8846(00)00351-3

Wen, S., & Chung, D. D. L. (2007). Electrical-resistance-based damage self-sensing in carbon fiber reinforced cement. *Carbon*, *45*(4), 710–716. http://dx.doi.org/10.1016/j.carbon.2006.11.029

Wenner, F. (1916). A method of measuring earth resistivity. *Bull Bur Stand*, *12*, 469. http://dx.doi.org/10.6028/bulletin.282

Whittington, H. W., McCarter, J., & Forde, M. C. (1981). The conduction of electricity through concrete. *Mag Concr Res*, *33*(114), 48–60. http://dx.doi.org/10.1680/macr.1981.33.114.48

Wiwattanachang N., & Giao, P. H. H. (2011). Monitoring crack development in fiber concrete beam by using electrical resistivity imaging. *J Appl Geophys*, *75*(2), 294–304. http://dx.doi.org/10.1016/j.jappgeo.2011.06.009

Yang, Z., Weiss, W. J., & Olek, J. (2006). Water transport in concrete damaged by tensile loading and freeze–thaw cycling. *J Mater Civ Eng*, *18*(3), 424–434. http://dx.doi.org/10.1061/(ASCE)0899-1561(2006)18:3(424)

Yang, Z., Weiss, W. J., Olek, J., & Nantung, T. (2005). Assessing damage, sorptivity, air content and strength of PCCP in Indiana. In *Proceedings of 8th International Conference on Concrete Pavements* (pp. 128–148). International Society for Concrete Pavements.

About the Joint Transportation Research Program (JTRP)

On March 11, 1937, the Indiana Legislature passed an act which authorized the Indiana State Highway Commission to cooperate with and assist Purdue University in developing the best methods of improving and maintaining the highways of the state and the respective counties thereof. That collaborative effort was called the Joint Highway Research Project (JHRP). In 1997 the collaborative venture was renamed as the Joint Transportation Research Program (JTRP) to reflect the state and national efforts to integrate the management and operation of various transportation modes.

The first studies of JHRP were concerned with Test Road No. 1—evaluation of the weathering characteristics of stabilized materials. After World War II, the JHRP program grew substantially and was regularly producing technical reports. Over 1,500 technical reports are now available, published as part of the JHRP and subsequently JTRP collaborative venture between Purdue University and what is now the Indiana Department of Transportation.

Free online access to all reports is provided through a unique collaboration between JTRP and Purdue Libraries. These are available at: http://docs.lib.purdue.edu/jtrp

Further information about JTRP and its current research program is available at: http://www.purdue.edu/jtrp

About This Report

An open access version of this publication is available online. This can be most easily located using the Digital Object Identifier (doi) listed below. Pre-2011 publications that include color illustrations are available online in color but are printed only in grayscale.

The recommended citation for this publication is:

Harris, D., Farnam, Y., Spragg, R., Imbrock, P., & Weiss, W. J. (2015). *Early detection of joint distress in portland cement concrete pavements* (Joint Transportation Research Program Publication No. FHWA/IN/JTRP-2015/09). West Lafayette, IN: Purdue University. http://dx.doi.org/10.5703/1288284315531